

# Lithosphere–asthenosphere Boundary Beneath the Sea of Japan From Transdimensional Inversion of S Receiver Functions

Takeshi Akuhara (✉ [akuhara@eri.u-tokyo.ac.jp](mailto:akuhara@eri.u-tokyo.ac.jp))

The University of Tokyo: Tokyo Daigaku <https://orcid.org/0000-0002-6129-8459>

**Kazuo Nakahigashi**

Tokyo University of Marine Science and Technology

**Masanao Shinohara**

University of Tokyo: Tokyo Daigaku

**Tomoaki Yamada**

University of Tokyo: Tokyo Daigaku

**Hajime Shiobara**

University of Tokyo: Tokyo Daigaku

**Yusuke Yamashita**

Kyoto University: Kyoto Daigaku

**Kimihiro Mochizuki**

University of Tokyo: Tokyo Daigaku

**Kenji Uehira**

National Research Institute for Earth Science and Disaster Resilience

---

## Full paper

**Keywords:** Back-arc basin, Lithosphere–asthenosphere boundary, Sea of Japan, S-receiver function, Transdimensional inversion, Ocean-bottom seismometer

**Posted Date:** May 18th, 2021

**DOI:** <https://doi.org/10.21203/rs.3.rs-523351/v1>

**License:** © ⓘ This work is licensed under a Creative Commons Attribution 4.0 International License.

[Read Full License](#)

---

1 **Lithosphere–asthenosphere boundary beneath the Sea of Japan from**  
2 **transdimensional inversion of S receiver functions**

3 Takeshi Akuhara<sup>1</sup>, akuhara@eri.u-tokyo.ac.jp

4 Kazuo Nakahigashi<sup>2</sup>, knakah0@kaiyodai.ac.jp

5 Masanao Shinohara<sup>1</sup>, mshino@eri.u-tokyo.ac.jp

6 Tomoaki Yamada<sup>1</sup>, yamada@eri.u-tokyo.ac.jp

7 Hajime Shiobara<sup>1</sup>, shio@eri.u-tokyo.ac.jp

8 Yusuke Yamashita<sup>3</sup>, yamac@rcep.dpri.kyoto-u.ac.jp

9 Kimihiro Mochizuki<sup>1</sup>, kimi@eri.u-tokyo.ac.jp

10 Kenji Uehira<sup>4</sup>, uehira@bosai.go.jp

11 <sup>1</sup> Earthquake Research Institute, The University of Tokyo, 1-1-1, Yayoi, Bunkyo-ku,

12 Tokyo 113-0032, Japan

13 <sup>2</sup> Department of Marine Resources and Energy, Tokyo University of Marine Science and

14 Technology, 4-5-7, Konan, Minato-ku, Tokyo 108-8477, Japan

15 <sup>3</sup> Miyazaki Observatory, Research Center for Earthquake Prediction, Disaster Prevention

16 Research Institute, Kyoto University, 3884, Kaeda, Miyazaki 889-2161, Japan

17 <sup>4</sup> National Research Institute for Earth Science and Disaster Resilience, 3-1, Tennodai,

18 Tsukuba-shi, Ibaraki 305-0006, Japan

19 Corresponding author: Takeshi Akuhara

20

21 **Abstract**

22 The evolution history of the Sea of Japan back-arc basin remains under debate,  
23 involving the opening of sub-basins such as the Japan and Yamato Basins. Detailed  
24 knowledge of the lithospheric structure will provide the key to understanding tectonic  
25 history. This study identifies the lithosphere–asthenosphere boundary (LAB) beneath  
26 the Sea of Japan back-arc basin using S-receiver functions (S-RFs). The study area,  
27 including the Japan and Yamato Basins, has been instrumented with broadband ocean-  
28 bottom seismometers (OBSs). S-RFs from these OBSs show negative  $S_p$  phases  
29 preceding the direct S arrivals, suggesting the LAB. The S-RFs also show abnormally  
30 reduced amplitudes. For further qualitative interpretation of these findings, we conduct  
31 transdimensional Bayesian inversion for S-wave velocity models. This less-subjective  
32 Bayesian approach clarifies that the low-velocity seafloor sediments and damped  
33 deconvolution contribute to the amplitude reduction, illuminating the necessity of such  
34 considerations for similar receiver function works. Inverted velocity structures show a  
35 sharp velocity decrease at the mantle depths, which we consider the LAB. The obtained  
36 LAB depths vary among sites: ~45 km beneath the Japan and Yamato Basins and ~70  
37 km beneath the Yamato Rise, a bathymetric high between the two basins. The thick  
38 lithosphere beneath the Yamato Rise most likely reflects its continental origin. However,

39 the thickness is still thin compared to that of eastern Asia, suggesting lithosphere  
40 extension by rifting. Notably, the Japan and Yamato Basins show a comparable  
41 lithospheric thickness, although the crustal thickness beneath the Yamato Basin is  
42 known to be anomalously thick. This consistency in the lithospheric thickness implies  
43 that both basins undergo similar back-arc opening processes.

44

45 **Keywords**

46 Back-arc basin

47 Lithosphere–asthenosphere boundary

48 Sea of Japan

49 S-receiver function

50 Transdimensional inversion

51 Ocean-bottom seismometer

52 **Background**

53 The Sea of Japan, located between the Japanese island-arc and Asia's eastern margin,  
54 hosts three sub-basins (Japan, Yamato, and Tsushima Basins) and a topographic high  
55 (the Yamato Rise) (**Figure 1**). The sea evolved through rifting and back-arc spreading,  
56 which have isolated Japanese Islands from Asia's continent. The rifting is likely to have  
57 begun at ~23 Ma, and the whole opening process ceases at ~15 Ma (Martin 2011; Van  
58 Horne et al. 2017), where clues come from various disciplines including radiometric  
59 dating for core samples (Tamaki et al. 1990), paleomagnetism from rocks (Otofuji et al.  
60 1985) and the seafloor (Seama and Isezaki 1990), dike, vein, and fault orientations (Sato  
61 1994), and migration of a volcanic front (Tatsumi et al. 1989). However, limited  
62 spatiotemporal resolution of these data makes the comprehensive understanding of the  
63 evolution process challenging. A major consensus is that back-arc spreading contributes  
64 to the formation of the Japan Basin, as is implied from the lineation pattern in the  
65 seafloor magnetic anomaly. In contrast, the formation processes of the Yamato and  
66 Tsushima basins are still open questions because of unclear magnetic anomaly and  
67 anomalous features of the crust, as introduced below.

68 Many active-source seismic surveys have revealed crustal structure at the Sea of Japan  
69 (Hirata et al. 1989; Kurashimo et al. 1996; Sato et al. 2006, 2018; Nakahigashi et al.

70 2013) and also have provided unique constraints on the evolution process. At the Japan  
71 Basin, the crust has a typical thickness of ~7 km for the oceanic crust, whereas the crust  
72 at the Yamato and Tsushima Basins is anomalously thick with a thickness of ~15 km.  
73 Although the origin is still puzzling, their relatively high P-wave velocities ( $V_p$ )  
74 resemble typical oceanic crusts than continental crusts (Sato et al. 2018). Hirata et al.  
75 (1989) has attributed the cause of this thickened crust to an excess magma supply after  
76 the termination of the seafloor spreading, which follows the abrupt tectonic reversal to  
77 the compressional field at ~15 Ma (Sato 1994). The Yamato Rise is a region with the  
78 thickest crusts in the sea with a thickness of ~25 km (Kurashimo et al. 1996; Kulinich  
79 and Valitov 2011). The lower  $V_p$  than the surrounding basins suggests that the rise is an  
80 extended, isolated continental crust (Kurashimo et al. 1996; Sato et al. 2018).

81 Revealing the lithospheric thickness, which is the first-order feature of the lithosphere  
82 structure, also benefits for better understanding the tectonics. Surface wave analyses  
83 have played that role for the Sea of Japan. The early studies by Abe & Kanamori (1970)  
84 and Evans et al. (1978) have estimated the averaged lithospheric thickness beneath the  
85 Sea of Japan to be ~30–40 km, using a few propagation paths crossing the sea of Japan.  
86 Modern surface wave tomography analyses with teleseismic sources (Yoshizawa et al.  
87 2010) and ambient noise (Zheng et al. 2011) have constructed 3D S-wave velocity ( $V_s$ )

88 models beneath the Sea of Japan. Both models identify a higher velocity of the  
89 lithosphere and a lower velocity of the asthenosphere with the transition occurring at  
90 ~50–70 km depth. However, the limited spatial resolution prohibits the precise  
91 determination of the lithosphere-asthenosphere boundary (LAB) depth, which is  
92 inherent to surface wave studies.

93 The S-receiver function (S-RF) analysis (e.g., Yuan et al. 2006) can reveal lithospheric  
94 thicknesses at a high spatial resolution by detecting Sp converted phases at the LAB.  
95 The method is advantageous over P receiver functions since the Sp converted phases are  
96 free from interferences by free-surface multiples. Because of its promised feature,  
97 numerous studies have employed this method to detect LAB (Kumar et al. 2005;  
98 Rychert et al. 2005; Lekic et al. 2011; Zhang et al. 2014; Hopper et al. 2020), and some  
99 of them have applied the method to the ocean-bottom environment (Kawakatsu et al.  
100 2009; Kumar et al. 2011; Rychert et al. 2018, 2021; Mark et al. 2021). However, the  
101 effects of unconsolidated sediments at the ocean bottom on S-RF waveforms has not  
102 been fully understood yet, which is another focus of this paper.

103 This study aims to constrain the LAB depths by applying the S-RF method to seven  
104 ocean-bottom seismometers (OBSs) deployed at the Japan and Yamato Basins and the  
105 Yamato Rise. We perform transdimensional inversion to interpret S-RFs as Vs structure

106 for three selected stations with good quality. Results indicate a thin lithosphere beneath  
107 the basins and a thick lithosphere beneath the Yamato Rise. Based on these results, we  
108 discuss the evolution process of the Sea of Japan.

109

## 110 **Data**

111 This study uses seismic waveform data from OBSs deployed at seven sites at the Sea of  
112 Japan: JS2, YMB3, and YMB4 located at the Yamato Basin; JPB4, JPB5, and JPB6 at  
113 the Japan Basin; and JS4 at the Yamato Rise (**Figure 1**). The observation periods differ  
114 from place to place. The intended observation period was one year or more for each site,  
115 but instrument malfunction limits data the lengths for JPB5 and JS2 to less than one  
116 year. The longest observation period is about two years. Table 1 summarizes the  
117 observation data analyzed by this study.

118 All seismometers mentioned above contain Güralp CMG-3T broadband sensors (Güralp  
119 Systems Ltd.) with a flat response at periods shorter than 360 s. Additionally, the series  
120 of temporary seismic observations involve deployments of short-period OBSs with a  
121 natural frequency of 1 Hz. Unfortunately, these short-period sensors prove to be  
122 ineffective in detecting clear onsets on teleseismic S waveforms. Thus, the present study  
123 only focuses on the data from the broadband OBSs. The orientations of horizontal

124 sensors are unknown because OBSs descend freely to the ocean bottom by gravity. The  
125 sensor orientations are estimated using the particle motion of Rayleigh waves (Stachnik  
126 et al. 2012).

127

## 128 **S receiver functions**

129 A seismically noisy environment in the ocean requires a visual inspection of the  
130 waveforms. S waveforms from teleseismic events with  $M > 5.5$  and epicentral distances  
131 of  $55\text{--}85^\circ$  undergo this visual inspection. Throughout this inspection, we consistently  
132 used a bandpass filter of  $0.03\text{--}0.1$  Hz to exclude the primary and secondary microseism  
133 bands and selected waveforms with clear onsets on the radial and vertical components.  
134 Figure 2 shows examples of S waveforms selected by this inspection. Out of 1218  
135 waveforms, 216 waveforms successfully passed this inspection.

136 For these selected waveforms, S-RFs are calculated by deconvolving the radial  
137 component from the vertical component. We use a spectral division with a damping  
138 factor for the deconvolution and apply a low-pass filter to the deconvolution results:

$$139 \quad SRF(t) = \frac{1}{\sqrt{2\pi}} \int_{-\infty}^{\infty} \frac{U_Z(\omega)U_R^*(\omega)}{U_R(\omega)U_R^*(\omega) + N_R(\omega)N_R^*(\omega)} LPF(\omega)\exp(i\omega t)d\omega, \quad (1)$$

140 where  $SRF(t)$  represents the time series of S-RF;  $U_Z(\omega)$  and  $U_R(\omega)$  represent  
141 vertical and radial component records in the frequency domain, respectively;  $N_R(\omega)$

142 represents a pre-signal record on the radial component (i.e., noise contribution); and the  
143 asterisk signifies complex conjugate. The low-pass filter,  $LPF(\omega)$ , is given by

$$144 \quad LPF(\omega) = \frac{1}{\sqrt{2}a} \exp\left(-\frac{\omega^2}{4a^2}\right). \quad (2)$$

145 Here, the factor  $a$  determines the cutoff frequency, which is set to 0.8. The  
146 normalization constant ( $1/\sqrt{2}a$ ) compensates for energy loss due to filtering, depending  
147 on the definition of the Fourier transform. Time windows for the deconvolution start  
148 and end 50 s before and 150 s after the direct S arrival, respectively. After the  
149 deconvolution, resultant S-RFs undergo time- and polarity-reversal for visualization  
150 purposes.

151 For further selecting S-RFs of good quality, we examine the waveform similarity  
152 between S-RFs from different teleseismic events. For each station, we calculate cross-  
153 correlation coefficients (CCs) between all S-RF pairs and retain S-RFs that show  
154 moderately high-similarity ( $CC > 0.35$ ) to more than half of all data. We find that this  
155 thresholding effectively rejects S-RFs with anomalous features, such as the base-line  
156 drift or high-frequency oscillation, especially for stations JPB4, JS4, and YMB3 (Figure  
157 3). Unfortunately, we were not able to retain adequate numbers of data for the other  
158 stations, which is due to short observation periods or high noise levels. For the three  
159 successful stations, we selected S-RFs and use the stacked waveform as the input data

160 for the subsequent inversion analysis (**Figure 3**, green lines).

161

## 162 **Transdimensional inversion**

163 To constrain the parameters of seismic velocity models, we perform transdimensional  
164 inversion of an S-RF waveform. This inversion method uses a reversible-jump Markov-  
165 chain Monte Carlo (RJMCMC) algorithm (Green 1995) that allows the number of  
166 unknowns to be unknown. The algorithm automatically determines the number of  
167 unknowns in a balance between the data fit and parsimony. This feature can reduce the  
168 subjectivity of the model parameter choice. For RF inversion, it can eliminate the  
169 subjective choice of the layer number. Many RF studies have used the RJMCMC  
170 algorithm for inverse problems in recent years (Piana Agostinetti and Malinverno 2010,  
171 2018; Akuhara et al. 2020). Some of them have performed joint inversion with surface  
172 wave dispersion curves (Bodin et al. 2012; Calò et al. 2016), whereas detailed inversion  
173 settings differ among studies. The following sections elaborate on specific setting in this  
174 study. Notably, one can reproduce the inversion setting of this paper using a computer  
175 program package, SEIS\_FILO (Akuhara 2021).

176 The goal of the RJMCMC algorithm is to sample the posterior probability distribution  
177 of the model parameters ( $\mathbf{m}_k$ ) and the hyperparameter ( $k$ ) under a condition of a given

178 data vector ( $\mathbf{d}$ ). Here, the model parameter vector  $\mathbf{m}_k$  has a variable dimension, which  
179 is a function of the hyperparameter  $k$ . According to Bayes' theorem, the posterior  
180 probability can be expressed as the product of a prior probability and a likelihood:

$$181 \quad P(k, \mathbf{m}_k | \mathbf{d}) = D \cdot P(k, \mathbf{m}_k) P(\mathbf{d} | k, \mathbf{m}_k), \quad (3)$$

182 where  $P(k, \mathbf{m}_k | \mathbf{d})$  is the posterior probability,  $P(k, \mathbf{m}_k)$  is the prior probability,  
183  $P(\mathbf{d} | k, \mathbf{m}_k)$  is the likelihood, and  $D$  is a normalization constant. For RF inversion,  
184 prior probability reflects our knowledge on subsurface structures, and likelihood  
185 indicates the goodness of waveform fit. Ambiguity in  $D$  hampers the direct calculation  
186 of the posterior probability using Equation 3. Instead, RJMCMC can simulate the  
187 probability through a random walk and a birth-death scheme.

### 188 *Model parameters*

189 We parameterize subsurface structure using the following hyperparameter and model  
190 parameters: the number of layers ( $k$ ), Vs perturbation of each layer ( $\delta\beta_i, i = 1 \cdots k$ ),  
191 and layer interface depths ( $z_i, i = 1 \cdots k - 1$ ). The velocity perturbation represents the  
192 difference from a reference velocity model. This reference model has smooth,  
193 increasing Vp and Vs with depth (**Figure 4**), which we manually made by referring to  
194 established Vp models from previous seismic surveys (Sato et al. 2004, 2018;  
195 Nakahigashi et al. 2013) and an empirical Vp–Vs relation (Brocher 2005). While Vs can

196 vary via parameters  $\delta\beta_i$ ,  $V_p$  is fixed at the value of the reference model. Density is  
 197 scaled to  $V_p$  with an empirical relation (Brocher 2005). For the seawater, the acoustic  
 198 velocity and density are assumed to be 1.5 km/s and 1.0 g/cm<sup>3</sup>, respectively.

### 199 ***Prior probability***

200 Assuming independence of model parameters, the prior probability,  $P(k, \mathbf{m}_k)$ , may be  
 201 expressed as

$$202 \quad P(k, \mathbf{m}_k) = P(k)P(z_1, \dots, z_k|k)P(\delta\beta_1, \dots, \delta\beta_{k+1}|k). \quad (4)$$

203 We assume a truncated uniform prior for the number of layers ( $k$ ), which is expressed  
 204 as:

$$205 \quad P(k) = \begin{cases} \frac{1}{k_{max} - k_{min}}, & k_{min} \leq k < k_{max}. \\ 0, & \text{else} \end{cases} \quad (5)$$

206  $k_{min}$  and  $k_{max}$  are set to 1 and 31, respectively, throughout this study. We also use a  
 207 non-informative prior for interface depths, which is given by

$$208 \quad P(z_1, \dots, z_k|k) = \begin{cases} \frac{k!}{(z_{max} - z_{min})^k}, & z_{min} \leq z_i \leq z_{max} \quad \text{for all } i = 1, \dots, k. \\ 0, & \text{else} \end{cases} \quad (6)$$

209 Equation 6 corresponds to the Dirichlet distribution, which assumes that the layer  
 210 interfaces are uniformly distributed over the range from  $z_{min}$  to  $z_{max}$  (Dosso et al.  
 211 2014). We set  $z_{min}$  and  $z_{max}$  to the sea depth and to 110 km, respectively.

212 For  $V_s$  perturbations, we use Gaussian distribution with a zero mean:

213 
$$P(\delta\beta_1 \cdots \delta\beta_{k+1} | k) = \prod_{i=1}^{k+1} \frac{1}{\sqrt{2\pi\sigma_{\delta\beta}^2}} \exp\left(-\frac{\delta\beta_i^2}{2\sigma_{\delta\beta}^2}\right), \quad (7)$$

214 where the standard deviation,  $\sigma_{\delta\beta}$ , reflects the reliability of the reference velocity  
 215 model. We set  $\sigma_{\delta\beta}$  to 0.4 km/s.

216 ***Likelihood***

217 We use a multivariate Gaussian distribution to formulate the likelihood:

218 
$$P(\mathbf{d} | k, \mathbf{m}_k) = \frac{1}{\sqrt{(2\pi)^N |\mathbf{C}|}} \exp\left[-\frac{1}{2} \{\mathbf{g}(k, \mathbf{m}_k) - \mathbf{d}\}^T \mathbf{C}^{-1} \{\mathbf{g}(k, \mathbf{m}_k) - \mathbf{d}\}\right]. \quad (8)$$

219 Here,  $\mathbf{C}$  is a covariance matrix and  $\mathbf{g}(k, \mathbf{m}_k)$  is a synthetic S-RF. The covariance  
 220 matrix is formulated as  $C_{ij} = \sigma^2 r^{(j-i)^2}$ , where  $\sigma$  is the standard deviation of the data  
 221 noise and  $r$  is the temporal correlation (Bodin et al. 2012). We fix  $\sigma$  at the time-  
 222 averaged value of the RF standard error obtained through the stacking process. We  
 223 associate the temporal correlation with the Gaussian low-pass filter via  $r =$   
 224  $\exp(-(\Delta t/2)^2)$ , where  $\Delta t$  represents the sampling interval.

225 A synthetic S-RF  $\mathbf{g}(k, \mathbf{m}_k)$  is computed by the propagator matrix method (Thomson  
 226 1950). The method allows us to fully consider the reverberated phases, even with a  
 227 water layer. The earth-flattening transformation is employed to account for the curvature  
 228 of the Earth. The calculated radial and vertical component seismograms are converted  
 229 into S-RFs through deconvolution, low-pass filtering, and time- and polarity-reversal.  
 230 For this deconvolution, we use a water-level damping with a factor of 0.001 (e.g.,

231 Clayton and Wiggins 1976). Here, the implemented deconvolution technique differs  
232 from what we use for the observation data for easy implementation.

233 ***Probabilistic sampling by reversible-jump Markov-chain Monte Carlo***

234 The RJMCMC iteratively explores a transdimensional model space through a random  
235 walk and a birth-death scheme. At every iteration, the RJMCMC proposes a new model  
236 ( $\mathbf{m}'_{k'}$ ) by modifying the model from the previous iteration ( $\mathbf{m}_k$ ). This modification  
237 includes adding a layer (a birth proposal;  $k' = k + 1$ ), removing a layer (a death  
238 proposal;  $k' = k - 1$ ), moving a layer interface ( $z'_i = z_i + \epsilon_z$ ), and perturbing Vs of a  
239 layer ( $\delta\beta'_i = \delta\beta_i + \epsilon_{\delta\beta}$ ). The amount of modification,  $\epsilon_z$  and  $\epsilon_{\delta\beta}$ , is extracted from  
240 a Gaussian distribution with a zero-mean and a standard deviation of 0.5 km and 0.2  
241 km/s, respectively. Adding the  $k'$ th layer requires setting properties of the new layer  
242 (i.e.,  $z_{k'}$  and  $\delta\beta_{k'}$ ). These properties are randomly determined using the same  
243 probability distribution as the prior probability (Dosso et al. 2014).

244 After the proposal, the RJMCMC judges a proposed model to be accepted or not using a  
245 Metropolis-Hastings-Green criterion (Green 1995; see Appendix 1). If the model is  
246 accepted, the accepted model is used in the next iteration to further make a new  
247 proposal. Otherwise, the previous model is held and used in the next iteration for a  
248 proposal. We perform 1,000,000 iterations, but the first 500,000 iterations are discarded

249 to avoid dependency on the initial state (so-called burn-in period). After this burn-in  
250 period, we save models at every 500th iterations to simulate the posterior probability  
251 distribution. We run 100 mutually interacted Markov-chains using a parallel tempering  
252 technique, which offers a more effective way of exploring a multidimensional space  
253 (Sambridge 2014; see Appendix 1).

## 254 **Results and interpretation**

255 Each inverted velocity structure shows a velocity decrease at the mantle depth, and the  
256 depths vary among sites (Figures 4–6). We interpret these velocity decreases as the  
257 LAB, a boundary between the high-velocity lithosphere and low-velocity  
258 asthenosphere. We qualitatively define the LAB depths as depths where the velocity  
259 starts decreasing, which follows 45 km depth beneath the Yamato Basin (station YMB3)  
260 and Japan Basin (station JPB4) and 70 km depth beneath the Yamato Rise (station JS4).  
261 The results also provide insights into the crustal thickness. The station YMB3 and JPB4  
262 exhibit evident velocity discontinuities at ~20 km and ~10 km depth, respectively.  
263 These discontinuities are most likely to represent the Moho. The thicker crust obtained  
264 beneath the Yamato Basin agrees with previous seismic surveys (Hirata et al. 1989; Sato  
265 et al. 2006, 2018; Nakahigashi et al. 2013). No sharp velocity discontinuity, potentially  
266 corresponding to the Moho, is observed for station JS4. Instead, the velocity gradually

267 increases to 30 km of depth. Considering a typical mantle  $V_s$  of  $\sim 4.6$  km/s, the Moho  
268 likely exists at 20–30 km depth. These estimated Moho depths roughly agree with  
269 seismic surveys.

270 Notably, all results indicate an extremely low  $V_s$  ( $< 1$  km/s) immediately beneath the  
271 seafloor, most likely reflecting water-saturated sediments. According to laboratory  
272 measurements, such slow velocities seem natural for water-saturated marine sediments  
273 (Hamilton 1979; Bowles 1997). Most seismic studies have rarely considered low-  
274 velocity sediments when they focus on mantle structures. However, we found that the  
275 low velocity is necessary and should not be ignored to explain overall reduced  
276 amplitudes in observed waveforms. We will provide further discussion for this  
277 statement in the following section. Below this layer, we obtain relatively higher  
278 velocities but still lower than 1.0 km/s. Further below, there exist layers with  $V_s > 1$   
279 km/s, which we considered as the crust.

280 We acknowledge that the sampled models underestimate the amplitudes of the negative  
281 peak seen in the observation. This underestimation can result from deconvolution. A  
282 damping factor stabilizing the deconvolution suppresses S-RF amplitudes under the  
283 presence of low-velocity sediments, which will be discussed in detail in the following  
284 section. Other possible causes of this underestimation are lateral heterogeneity,

285 including dipping layer interfaces and anisotropy. Unevenly distributed teleseismic  
286 events, mostly from the Tonga-Kermadec subduction zone, likely prohibit such a  
287 dipping layer or anisotropy effect from diminishing through stacking. Whatever the  
288 cause, this amplitude underestimation could distort the estimations of the velocity  
289 contrast at the LAB. The LAB depths would be less susceptible to this effect because the  
290 predicted waveforms explain the peak locations well.

291

## 292 **Discussion**

### 293 *Contribution of sediment to S-receiver functions*

294 Though not the center of focus, our inversion analysis has predicted thin, low-velocity  
295 layers at the top of the resulting models. This prediction may seem peculiar because  
296 low-frequency waveforms ( $< 0.1$  Hz) are usually insensitive to thin layers. Another  
297 peculiarity lies in the considerably small amplitudes of the observed S-RFs, which are  
298  $\sim 20\%$  of the ordinary expectation. Understanding these peculiarities seems essential to  
299 appreciate our inversion results. The following paragraphs provide a unified explanation  
300 for these features, where spectral notches caused by sediment reverberations play a role.  
301 The sediment reverberations are inherent in ocean environments. Thus, insights  
302 presented here will be suited to other offshore S-RF studies.

303 Consider simple structure models consisting of water, sediment, and mantle layers, with  
304 varying sediment  $V_s$  (**Figure 8a**). Synthetic S-RFs by the propagator matrix method and  
305 the water-level deconvolution exhibit decreasing amplitudes with an increasing velocity  
306 contrast at the sediment–mantle interface. The degree of this suppression depends on a  
307 damping factor imposed on the deconvolution (**Figure 8b–d**). Without damping, where  
308 the amplitude reduction mostly reflects a magnified S-to-S transmission coefficient at  
309 the interface, we only obtain a slight peak reduction to  $\sim 0.35$  even for the extreme case  
310 (**Figure 8b**). This trivial reduction ( $\sim 30\%$ ) is insufficient to explain the observed  
311 amplitude reduction ( $\sim 80\%$ ). A damping factor added to a deconvolution denominator  
312 exerts a more significant control over the S-RF amplitudes and allows the reproduction  
313 of the observed peak amplitudes (**Figure 8c, d**). This tendency still holds even if we  
314 employ more complex, realistic velocity models (**Figure 8e–h**).

315 Algebraic formulation of the reverberation phases offers further insight into the  
316 damping effects. Assume a simple water-sediment-mantle model (**Figure 8a**) and a  
317 vertical incidence of a teleseismic S waveform to the model. The power spectrum of the  
318 radial-component response, given by Equation 18 in Appendix 2, has spectral notches,  
319 and the notch depths increase with an increasing velocity contrast at the interface  
320 (**Figure 9a**). At a higher velocity contrast, such "deep" notches are more likely subjected

321 to damping effects. For the observation data, high-level noise can also fill in these  
322 notches. Such a spectral fill in will increase the denominator of deconvolution and thus  
323 reduce S-RF amplitudes. **Figure 9b** confirms this situation through a numerical  
324 calculation using the propagator matrix method, which considers an oblique incidence  
325 of a waveform and includes secondary effects such as P-to-S conversions and the sea  
326 water layer. The resultant spectrum still indicates similar spectral notches to algebraic  
327 ones.

328 The above discussion implies a tradeoff between the sediment Vs and the damping  
329 value. Our arbitral selection of the damping factor during inversion possibly biases the  
330 estimated sediment Vs (and their thicknesses), but we found that this choice does not  
331 affect LAB depths drastically. We acknowledge that we employed different damping  
332 schemes for the observed and synthetic S-RF calculations (frequency-dependent  
333 damping vs. constant water-level damping). Effects from various damping schemes  
334 should be investigated in the future. Alternatively, deconvolution may be avoided using  
335 transfer function-based techniques (Bodin et al. 2014; Frederiksen and Delaney 2015;  
336 Akuhara et al. 2019).

### 337 *Lateral variation in lithospheric structure*

338 We have performed the inversion analysis for three good-conditioned stations, and the

339 results show the thickest lithosphere beneath the Yamato Rise. Here, we argue that S-  
340 RFs from the other stations qualitatively support this finding. **Figure 10** shows a stack  
341 of time-to-depth converted S-RFs at each station, including S-RFs rejected by the CC  
342 criteria. We converted time to depth using the three median models from the inversion  
343 results (Blue lines in Figures 5–7), assuming a laterally homogeneous structure across  
344 each tectonic domain, i.e., we use the JPB4 model for migrating JPB4, JPB5, and JPB6  
345 data; the YMB3 model for YMB3, YMB4, and JS2 data; and the JS4 model for JS4  
346 data. All stacked receiver functions show a significant negative peak representing the  
347 LAB (**Figure 10b**). The exact depths are hard to estimate from this stacking because of  
348 the broadened peak. Nevertheless, the results still imply the thickest lithosphere beneath  
349 the Yamato Rise and a relatively constant thickness beneath the surrounding basins.

350 An independent surface wave tomography study (Yoshizawa et al. 2010) also indicates  
351 the thickened lithosphere beneath the Yamato Rise (**Figure 11**). Their model shows a  
352 high  $V_s$  zone at shallow mantle depths (30–60 km) beneath the Yamato Rise (**Figure**  
353 **11b**), and its lateral extent roughly corresponds to that of the topographic high (**Figure**  
354 **11a**). A strong velocity contrast resides around 60–80 km depth, which agrees with our  
355 inverted model. The contrast becomes relatively obscure further southward, beneath the  
356 Yamato Basin. However, our estimated LAB depth (45 km beneath the YMB3) seems

357 consistent with their model.

358 The depth-converted S-RFs in **Figure 10** also offer implications on the crustal  
359 thickness. The first positive peak can represent the combination of S-to-P converted  
360 phases from the sediment-crust, intra-crust, and Moho discontinuities, and thus, its peak  
361 width will roughly correspond to the crustal thickness. Consequently, the results  
362 indicate the thickest crustal thickness beneath the Yamato Rise, moderate thicknesses  
363 beneath the Yamato Basin, and thin thicknesses beneath the Japan Basin. This first-order  
364 feature is consistent with active-source seismic surveys (Hirata et al. 1989; Sato et al.  
365 2004, 2018, 2020; Nakahigashi et al. 2013). Interestingly, the Yamato and Japan Basins  
366 seem to have comparable LAB depths, as suggested from inversion results. This  
367 similarity contrasts with the observed variation in crustal thicknesses. We further  
368 discuss this point in the subsequent section.

### 369 *Tectonic implications*

370 This study has identified the LAB beneath the Sea of Japan back-arc basin. Results have  
371 shown (1) thick lithosphere beneath the Yamato Rise and (2) a comparable lithosphere  
372 thickness beneath the Yamato and Japan Basins. Whereas an ambient noise tomographic  
373 study has implied a similar feature (Zheng et al. 2011), our S-RF analysis has  
374 emphasized it through its high-resolution constraints. This section describes tectonic

375 implications from the obtained first-order features of the lithosphere. **Figure 12**  
376 schematically shows our interpretations.

377 Many studies assume that the Yamato Rise is a continental fragment isolated from the  
378 Asia continent (Tamaki 1985; e.g., Kurashimo et al. 1996). The crustal  $V_p$  has  
379 supported this hypothesis, which is lower than typical velocities for oceanic crusts (Sato  
380 et al. 2018). Tectonic reconstruction models suggest that the Yamato Rise lies adjacent  
381 to the Sikhote Alin at the pre-rift stage (Kim et al. 2007). In the vicinity, northeastern  
382 China, an S-RF study has identified the LAB at  $\sim 150$  km depth (Zhang et al. 2014),  
383 which may roughly indicate the original lithosphere thickness beneath the Yamato Rise.  
384 Considering the current LAB depth  $\sim 70$  km obtained by this study, the lithosphere may  
385 undergo lateral extension by a factor of  $\sim 2$  through the rifting process. Such an  
386 extension can induce normal faulting in the crust and contribute to trough formation,  
387 which appears in the seafloor topography.

388 The origin of the Yamato Basin, which has an anomalously thick crust, is under debate.  
389 Some studies interpreted the crust as an extended continental crust, whereas others as a  
390 thickened oceanic crust. In contrast, there is no doubt that the seafloor spreading is the  
391 origin of the Japan Basin, judging from the lineation pattern in the seafloor magnetic  
392 anomaly (Seama and Isezaki 1990). The estimated velocity structures with comparable

393 LAB depths may imply that the Yamato Basin also originates from the seafloor  
394 spreading like the Japan Basin, assuming that the LAB depths primarily reflect the  
395 thermal state and thus depend on the age (Stein and Stein 1996; Kawakatsu et al. 2009;  
396 Schmerr 2012). Note that the two basins have similar ages of 19 – 20 Myr (Kaneoka et  
397 al. 1992). We argue that our estimated lithospheric thickness (~45 km) agrees with  
398 observations from other ocean regions with similar lithospheric ages (Rychert et al.  
399 2020 and references therein). Our results do not exclude the possibility that the  
400 lithospheric extension has formed the Yamato Basin. However, if this true, there would  
401 be no anticipation that both basins show consistent thicknesses.

402 Whereas we have observed evident indicators of the LAB from S-to-P converted phases  
403 across a wide area of the Sea of Japan (Figures 5–7 and 10), there is no observable LAB  
404 reported beneath the Japanese Islands. Mantle upwelling flow, related to volcanisms  
405 (Nakajima et al. 2001; Nakajima and Hasegawa 2007), can thermally or mechanically  
406 complicate structures at the depth and may obscure the clear LAB manifestation. The  
407 coherent Sp phase observed beneath the Sea of Japan suggests a mechanically strong  
408 lithosphere, whereas the lithosphere likely becomes weak beneath the Japanese Islands  
409 because of the volcanisms. Such contrast will be of importance for considering  
410 seismogenesis around Japan. For instance, a seismogenic belt in the eastern margin of

411 the Sea of Japan, running sub-parallel to the Japanese Island (Fukao and Furumoto  
412 1975), may be attributed to strain accumulated near the transition between the strong  
413 and weak lithosphere.

414 A limitation of this study lies in the sparse distribution of OBSs. So far, there has been  
415 no passive seismic monitoring conducted at the Tsushima Basin. Such observation  
416 would help gain further insights into the tectonics of the Sea of Japan. Owing to its  
417 similar crustal features to the Yamato Basin, identifying the LAB depth beneath the  
418 Tsushima Basin may (or may not) support our interpretation for the Yamato Basin.  
419 Additionally, it could also help better understand interseismic deformation of the  
420 southwestern Japan toward future megathrust earthquakes through kinematic modeling.

421

## 422 **Conclusion**

423 This study investigated the lithospheric structure beneath the Sea of Japan through  
424 inversion of S-RF waveforms derived from the OBS data. Inverted structures show a  
425 velocity decrease in the mantle depths, and we conclude the LAB is located at ~45 km  
426 depth beneath the Japan and Yamato Basins and ~65 km beneath the Yamato Rise. The  
427 deepened LAB beneath the rise most likely reflects its continental origin, but the depth  
428 is still shallower than that beneath northeastern China, suggesting lithospheric

429 extension. The obtained comparable LAB depths for the Japan and Yamato Basins  
430 indicate that both basins share a common tectonic origin: the back-arc spreading. The  
431 origin of the enigmatic Yamato Basin has been controversial, and many active-source  
432 seismic surveys have investigated shallow crustal structures for clues. This study offers  
433 an additional constraint, for the first time, from the deeper lithospheric structure, which  
434 owes to the high-resolution feature of receiver functions.

435 This study also discusses technical issues of S-RFs at the ocean bottom. As an  
436 explanation of observed abnormally reduced amplitudes, we propose a theoretical  
437 perspective on how sediment reverberations and additive damping (or noise) to the  
438 deconvolution denominator can reduce S-RF amplitudes. However, our treatment of this  
439 issue may not be sufficient, as implied by systematic overestimation of S-RF  
440 amplitudes. This point should be further investigated in the future, which renders S-RF  
441 methods using OBS data a more promising tool to decipher the lithosphere–  
442 asthenosphere system.

443

#### 444 **Appendix 1. Acceptance criteria and parallel tempering**

445 The RJMCMC algorithm aims to extract samples from model spaces such that samples  
446 follow their posterior probability. Each proposed model needs to be accepted or rejected

447 under the equilibrium condition. For a fixed dimension (i.e.,  $k = \text{constant}$ ), this  
 448 condition can be met by accepting proposed models with the probability given by the  
 449 Metropolis-Hastings criterion:

$$450 \quad \alpha_{MH}(k, \mathbf{m}'_k | k, \mathbf{m}_k) = \min \left[ 1, \frac{P(k, \mathbf{m}')}{P(k, \mathbf{m})} \cdot \frac{P(\mathbf{d}|k, \mathbf{m}'_k)}{P(\mathbf{d}|k, \mathbf{m}_k)} \cdot \frac{Q(\mathbf{m}_k | \mathbf{m}'_k)}{Q(\mathbf{m}'_k | \mathbf{m}_k)} \right]. \quad (9)$$

451 Here,  $\mathbf{m}_k$  and  $\mathbf{m}'_k$  are the last-accepted and proposed models, respectively; and  
 452  $Q(\mathbf{m}'_k | \mathbf{m}_k)$  is the probability that a random walk from  $\mathbf{m}_k$  to  $\mathbf{m}'_k$  occurs. Our setting  
 453 simplifies Equation 9 because of the symmetricity of a random walk (i.e.,

$$454 \quad Q(\mathbf{m}'_k | \mathbf{m}_k) = Q(\mathbf{m}_k | \mathbf{m}'_k):$$

$$455 \quad \alpha_{MH}(k, \mathbf{m}'_k | k, \mathbf{m}_k) = \min \left[ 1, \frac{P(k, \mathbf{m}')}{P(k, \mathbf{m})} \cdot \frac{P(\mathbf{d}|k, \mathbf{m}'_k)}{P(\mathbf{d}|k, \mathbf{m}_k)} \right]. \quad (10)$$

456 Equations 9 and 10 assume that the model space dimension does not change through  
 457 a random walk. Green (1995) has introduced the Metropolis-Hastings-Green criterion  
 458 that can account for the dimensional change:

$$459 \quad \alpha_{MHG}(k', \mathbf{m}'_{k'} | k, \mathbf{m}_k) = \min \left[ 1, \frac{P(k', \mathbf{m}'_{k'})}{P(k, \mathbf{m}_k)} \cdot \frac{P(\mathbf{d}|k', \mathbf{m}'_{k'})}{P(\mathbf{d}|k, \mathbf{m}_k)} \cdot \frac{Q(k, \mathbf{m}_k | k', \mathbf{m}'_{k'})}{Q(k', \mathbf{m}'_{k'} | k, \mathbf{m}_k)} \cdot |\mathbf{J}| \right]. \quad (11)$$

460 The Jacobian  $|\mathbf{J}|$  in Equation 11 adjusts unit volume change in the model space.

461 Specific configurations of a random walk are known to cancel out similar terms in

462 Equation 11 (Dosso et al. 2014; Sen and Biswas 2017), leading to

$$463 \quad \alpha_{MHG}(k', \mathbf{m}'_{k'} | k, \mathbf{m}_k) = \min \left[ 1, \frac{P(\mathbf{d}|k', \mathbf{m}'_{k'})}{P(\mathbf{d}|k, \mathbf{m}_k)} \right]. \quad (12)$$

464 To enhance the efficiency of model sampling, the parallel tempering technique (Geyer

465 and Thompson 1995; Sambridge 2014) introduces an additional parameter representing  
 466 temperature ( $T_i$ ) to Equations 10 and 12:

$$467 \quad \alpha_{MH}(k, \mathbf{m}'_k | k, \mathbf{m}_k) = \min \left[ 1, \frac{P(k, \mathbf{m}')}{P(k, \mathbf{m})} \cdot \left\{ \frac{P(\mathbf{d} | k, \mathbf{m}'_k)}{P(\mathbf{d} | k, \mathbf{m}_k)} \right\}^{\frac{1}{T_i}} \right] \quad (13)$$

468 and

$$469 \quad \alpha_{MHG}(k', \mathbf{m}'_{k'} | k, \mathbf{m}_k) = \min \left[ 1, \left\{ \frac{P(\mathbf{d} | k', \mathbf{m}'_{k'})}{P(\mathbf{d} | k, \mathbf{m}_k)} \right\}^{\frac{1}{T_i}} \right]. \quad (14)$$

470 Higher temperatures than unity lose the acceptance criterion to accept more models.

471 Such tempered chains can walk through the broader region in the model space

472 consequently. However, this modification by  $T_i$  breaks the equilibrium condition, and

473 thus the sampled model does not simulate the posterior probability distribution. The

474 parallel tempering technique remedies this issue by running 100 MCMC chains with

475 different temperature ( $T_i; i = 1 \dots 100$ ) in parallel. At each iteration, two chains are

476 arbitrarily selected, and their temperatures are swapped with a probability of

$$477 \quad \alpha_{PT}(i, j) = \min \left[ 1, \left\{ \frac{P(\mathbf{d} | k^j, \mathbf{m}_{kj}^j)}{P(\mathbf{d} | k^i, \mathbf{m}_{ki}^i)} \right\}^{\frac{1}{T_i}} \left\{ \frac{P(\mathbf{d} | k^i, \mathbf{m}_{ki}^i)}{P(\mathbf{d} | k^j, \mathbf{m}_{kj}^j)} \right\}^{\frac{1}{T_j}} \right], \quad (15)$$

478 where superscripts  $i, j$  represent the indices for MCMC chains. Equation 15

479 guarantees that this temperature swap meets the equilibrium condition. The posterior

480 probability can be retrieved by gathering models accepted with non-tempered chains.

481 Our inversion involves 20 chains having a unit temperature (i.e., non-tempered). For  
 482 the other 80 chains, we randomly set temperatures, which range from 1 to 20.

483

## 484 **Appendix 2. Algebraic expression for sediment reverberations**

485 When a plane, impulsive, unit-amplitude, upgoing, nearly-vertical SV waveform  
 486 incidents to this structure model, a radial-component elastic response at the sediment  
 487 top is approximately given by

$$488 \quad u_r(t) = f_s \hat{S} \hat{S}' \left[ \sum_{n=0}^{\infty} (-r)^n \delta(t - n\tau) \right], \quad f_s = 2, \quad \hat{S} \hat{S}' = 1 + \hat{S} \hat{S}',$$

$$\tau = \frac{2h_1}{\beta_1}, \quad \hat{S} \hat{S}' = \frac{\rho_2 \beta_2 - \rho_1 \beta_1}{\rho_1 \beta_1 + \rho_2 \beta_2}$$
(16)

489 in the time domain and

$$490 \quad U_R(\omega) = 2(1 + \hat{S} \hat{S}') \frac{1}{(1 + \hat{S} \hat{S}' e^{-i\omega\tau})}$$
(17)

491 in the frequency domain (Yu et al. 2015), where  $h_1$ ,  $\beta_1$ , and  $\rho_1$  represent a thickness,  
 492  $V_s$ , and a density of the overriding sediment layer, respectively;  $\beta_2$  and  $\rho_2$  represent  
 493  $V_s$  and a density of the half space;  $f_s$  represents free-surface reflection;  $\tau$  represents a  
 494 two-way travel time of S-wave passing through the sediment layer; and  $\hat{S} \hat{S}'$  and  $\hat{S} \hat{S}'$   
 495 represent reflection and transmission coefficients at the layer interface, respectively.

496 From equation 17, we obtain the denominator of deconvolution without damping:

$$497 \quad U_R(\omega) U_R^*(\omega) = \frac{2(1 + \hat{S} \hat{S}')^2}{1 + \hat{S} \hat{S}' \cos(\tau\omega)}$$
(18)

498 **Availability of data and materials**

499 The teleseismic waveforms analyzed during this study are available from the  
500 corresponding author on reasonable request.

501 **Competing interests**

502 The authors declare no competing interests.

503 **Funding**

504 This study was conducted as a part of Integrated Research Project on Seismic and  
505 Tsunami Hazards around the Sea of Japan by the Ministry of Education, Culture, Sports,  
506 Science, and Technology (MEXT) of Japan.

507 **Authors' contributions**

508 TA analyzed waveform data. TA, KN, and MS interpreted the data and designed the  
509 seismic observation. All authors contribute to the data acquisition and read and  
510 approved the final manuscript.

511 **Acknowledgments**

512 We thank Kazunori Yoshizawa for providing the tomography model of the Sea of Japan.

513

514 **References**

515 Abe K, Kanamori H (1970) Mantle structure beneath the Japan Sea as

516 revealed by surface waves. Bull Earthq Res Institute, Univ Tokyo 48:1011–1021

517 Akuhara T (2021) SEIS\_FILO: seismological transdimensional inversion  
518 tools for flat and isotropic layered structure in the ocean

519 Akuhara T, Bostock MGMG, Plourde APAP, Shinohara M (2019) Beyond  
520 Receiver Functions: Green’s Function Estimation by Transdimensional Inversion  
521 and Its Application to OBS Data. J Geophys Res Solid Earth 124:1944–1961. doi:  
522 10.1029/2018JB016499

523 Akuhara T, Tsuji T, Tonegawa T (2020) Overpressured Underthrust  
524 Sediment in the Nankai Trough Forearc Inferred From Transdimensional Inversion  
525 of High-Frequency Teleseismic Waveforms. Geophys Res Lett 47:. doi:  
526 10.1029/2020GL088280

527 Bodin T, Sambridge M, Tkalčić H, et al (2012) Transdimensional inversion  
528 of receiver functions and surface wave dispersion. J Geophys Res Solid Earth  
529 117:1–24. doi: 10.1029/2011JB008560

530 Bodin T, Yuan H, Romanowicz B (2014) Inversion of receiver functions  
531 without deconvolution—application to the Indian craton. Geophys J Int 196:1025–  
532 1033. doi: 10.1093/gji/ggt431

533 Bowles FA (1997) Observations on attenuation and shear-wave velocity in

534 fine-grained, marine sediments. *J Acoust Soc Am* 101:3385–3397. doi:  
535 10.1121/1.419374

536 Brocher TM (2005) Empirical relations between elastic wavespeeds and  
537 density in the Earth’s crust. *Bull Seismol Soc Am* 95:2081–2092. doi:  
538 10.1785/0120050077

539 Calò M, Bodin T, Romanowicz B (2016) Layered structure in the upper  
540 mantle across North America from joint inversion of long and short period seismic  
541 data. *Earth Planet Sci Lett* 449:164–175. doi: 10.1016/j.epsl.2016.05.054

542 Clayton RW, Wiggins RA (1976) Source shape estimation and  
543 deconvolution of teleseismic body waves. *Geophys J R Astron Soc* 151–177

544 Dosso SE, Dettmer J, Steininger G, Holland CW (2014) Efficient trans-  
545 dimensional Bayesian inversion for geoacoustic profile estimation. *Inverse Probl*  
546 30:114018. doi: 10.1088/0266-5611/30/11/114018

547 Evans JR, Suyehiro K, Sacks IS (1978) Mantle structure beneath the Japan  
548 Sea—A re-examination. *Geophys Res Lett* 5:487–490. doi:  
549 10.1029/GL005i006p00487

550 Frederiksen AW, Delaney C (2015) Deriving crustal properties from the P  
551 Coda without deconvolution: The southwestern Superior Province, North America.

552 Geophys J Int 201:1491–1506. doi: 10.1093/gji/ggv086

553 Fukao Y, Furumoto M (1975) Mechanism of large earthquakes along the  
554 eastern margin of the Japan sea. Tectonophysics 26:247–266. doi: 10.1016/0040-  
555 1951(75)90093-1

556 Geyer CJ, Thompson EA (1995) Annealing Markov Chain Monte Carlo with  
557 Applications to Ancestral Inference. J Am Stat Assoc 90:909–920. doi:  
558 10.1080/01621459.1995.10476590

559 Green PJ (1995) Reversible jump Markov chain monte carlo computation  
560 and Bayesian model determination. Biometrika 82:711–732. doi:  
561 10.1093/biomet/82.4.711

562 Hamilton EL (1979)  $V_p / V_s$  and Poisson's ratios in marine sediments  
563 and rocks. J Acoust Soc Am 66:1093–1101. doi: 10.1121/1.383344

564 Hirata N, Tokuyama H, Chung TW (1989) An anomalously thick layering of  
565 the crust of the yamato basin, southeastern sea of japan: the final stage of back-arc  
566 spreading. Tectonophysics 165:303–314. doi: 10.1016/0040-1951(89)90055-3

567 Hopper E, Gaherty JB, Shillington DJ, et al (2020) Preferential localized  
568 thinning of lithospheric mantle in the melt-poor Malawi Rift. Nat Geosci 13:584–  
569 589. doi: 10.1038/s41561-020-0609-y

570 Kaneoka I, Takigami Y, Takaoka N, et al (1992)  $^{40}\text{Ar}$ - $^{39}\text{Ar}$  Analysis of  
571 Volcanic Rocks Recovered from the Japan Sea Floor: Constraints on the Age of  
572 Formation of the Japan Sea. In: Proceedings of the Ocean Drilling Program,  
573 127/128 Part 2 Scientific Results. Ocean Drilling Program, pp 819–836

574 Kawakatsu H, Kumar P, Takei Y, et al (2009) Seismic Evidence for Sharp  
575 Lithosphere-Asthenosphere Boundaries of Oceanic Plates. *Science* (80- ) 324:499–  
576 502. doi: 10.1126/science.1169499

577 Kim HJ, Lee GH, Jou HT, et al (2007) Evolution of the eastern margin of  
578 Korea: Constraints on the opening of the East Sea (Japan Sea). *Tectonophysics*  
579 436:37–55. doi: 10.1016/j.tecto.2007.02.014

580 Kulinich RG, Valitov MG (2011) Thicknesses and types of the crust beneath  
581 the Sea of Japan inferred from marine and satellite gravimetric investigations. *Russ*  
582 *J Pacific Geol* 5:481–491. doi: 10.1134/S1819714011060078

583 Kumar P, Kawakatsu H, Shinohara M, et al (2011) P and S receiver function  
584 analysis of seafloor borehole broadband seismic data. *J Geophys Res Solid Earth*  
585 116:1–17. doi: 10.1029/2011JB008506

586 Kumar P, Yuan X, Kind R, Kosarev G (2005) The lithosphere-asthenosphere  
587 boundary in the Tien Shan-Karakoram region from S receiver functions: Evidence

588 for continental subduction. *Geophys Res Lett* 32:1–4. doi: 10.1029/2004GL022291

589 Kurashimo E, Shinohara M, Suyehiro K, et al (1996) Seismic evidence for  
590 stretched continental crust in the Japan Sea. *Geophys Res Lett* 23:3067–3070. doi:  
591 10.1029/96GL02765

592 Lekic V, French SW, Fischer KM (2011) Lithospheric Thinning Beneath  
593 Rifted Regions of Southern California. *Science* (80- ) 334:783–787. doi:  
594 10.1126/science.1208898

595 Mark HF, Collins JA, Lizarralde D, et al (2021) Constraints on the Depth,  
596 Thickness, and Strength of the G Discontinuity in the Central Pacific From S  
597 Receiver Functions. *J Geophys Res Solid Earth* 126:e2019JB019256. doi:  
598 10.1029/2019JB019256

599 Martin AK (2011) Double saloon door tectonics in the Japan Sea, Fossa  
600 Magna, and the Japanese Island Arc. *Tectonophysics* 498:45–65. doi:  
601 10.1016/j.tecto.2010.11.016

602 Nakahigashi K, Shinohara M, Yamada T, et al (2013) Seismic structure of  
603 the extended continental crust in the Yamato Basin, Japan Sea, from ocean bottom  
604 seismometer survey. *J Asian Earth Sci* 67–68:199–206. doi:  
605 10.1016/j.jseaes.2013.02.028

606 Nakajima J, Hasegawa A (2007) Tomographic evidence for the mantle  
607 upwelling beneath southwestern Japan and its implications for arc magmatism.  
608 Earth Planet Sci Lett 254:90–105. doi: 10.1016/j.epsl.2006.11.024

609 Nakajima J, Matsuzawa T, Hasegawa A, Zhao D (2001) Junichi Nakajima,  
610 Toru Matsuzawa, and Akira Hasegawa. J Geophys Res 106:21843–21857

611 Otofuji Y-I, Matsuda T, Nohda S (1985) Opening mode of the Japan Sea  
612 inferred from the palaeomagnetism of the Japan Arc. Nature 317:603–604. doi:  
613 10.1038/317603a0

614 Piana Agostinetti N, Malinverno A (2010) Receiver function inversion by  
615 trans-dimensional Monte Carlo sampling. Geophys J Int 181:858–872. doi:  
616 10.1111/j.1365-246X.2010.04530.x

617 Piana Agostinetti N, Malinverno A (2018) Assessing uncertainties in high-  
618 resolution, multifrequency receiver-function inversion: A comparison with  
619 borehole data. Geophysics 83:KS11–KS22. doi: 10.1190/geo2017-0350.1

620 Rychert CA, Fischer KM, Rondenay S (2005) A sharp lithosphere–  
621 asthenosphere boundary imaged beneath eastern North America. Nature 436:542–  
622 545. doi: 10.1038/nature03904

623 Rychert CA, Harmon N, Constable S, Wang S (2020) The Nature of the

624 Lithosphere-Asthenosphere Boundary. *J Geophys Res Solid Earth* 125:1–39. doi:  
625 10.1029/2018JB016463

626 Rychert CA, Harmon N, Tharimena S (2018) Scattered wave imaging of the  
627 oceanic plate in cascadia. *Sci Adv* 4:1–8. doi: 10.1126/sciadv.aao1908

628 Rychert CA, Tharimena S, Harmon N, et al (2021) A dynamic lithosphere–  
629 asthenosphere boundary near the equatorial Mid-Atlantic Ridge. *Earth Planet Sci*  
630 *Lett* 566:116949. doi: 10.1016/j.epsl.2021.116949

631 Sambridge M (2014) A Parallel Tempering algorithm for probabilistic  
632 sampling and multimodal optimization. *Geophys J Int* 196:357–374. doi:  
633 10.1093/gji/ggt342

634 Sato H (1994) stress field and basin development in northeast Japan stress.  
635 *Geophys Res* 99:

636 Sato T, No T, Arai R, et al (2020) Transition from continental rift to back-  
637 arc basin in the southern Japan Sea deduced from seismic velocity structures.  
638 *Geophys J Int* 221:722–739. doi: 10.1093/gji/ggaa006

639 Sato T, No T, Miura S, Kodaira S (2018) Crustal characteristic variation in  
640 the central Yamato Basin, Japan Sea back-arc basin, deduced from seismic survey  
641 results. *Tectonophysics* 726:1–13. doi: 10.1016/j.tecto.2018.01.022

642 Sato T, Shinohara M, Karp BY, et al (2004) P-wave velocity structure in the  
643 northern part of the central Japan Basin, Japan Sea with ocean bottom  
644 seismometers and airguns. *Earth, Planets Sp* 56:501–510. doi:  
645 10.1186/BF03352509

646 Sato T, Takahashi N, Miura S, et al (2006) Last stage of the Japan Sea back-  
647 arc opening deduced from the seismic velocity structure using wide-angle data.  
648 *Geochemistry, Geophys Geosystems* 7:. doi: 10.1029/2005GC001135

649 Schmerr N (2012) The Gutenberg Discontinuity: Melt at the Lithosphere-  
650 Asthenosphere Boundary. *Science* (80- ) 335:1480–1483. doi:  
651 10.1126/science.1215433

652 Seama N, Isezaki N (1990) Sea-floor magnetization in the eastern part of the  
653 Japan Basin and its tectonic implications. *Tectonophysics* 181:285–297. doi:  
654 10.1016/0040-1951(90)90022-Z

655 Sen MK, Biswas R (2017) Transdimensional seismic inversion using the  
656 reversible jump Hamiltonian Monte Carlo algorithm. *Geophysics* 82:R119–R134.  
657 doi: 10.1190/geo2016-0010.1

658 Stachnik JC, Sheehan AF, Zietlow DW, et al (2012) Determination of New  
659 Zealand Ocean Bottom Seismometer Orientation via Rayleigh-Wave Polarization.

660 Seismol Res Lett 83:704–713. doi: 10.1785/0220110128

661 Stein S, Stein CA (1996) Thermo-Mechanical Evolution of Oceanic  
662 Lithosphere: Implications for the Subduction Process and Deep Earthquakes.  
663 Subduction Top to Bottom Geophys Monogr 96:1–17. doi: 10.1029/GM096p0001

664 Tamaki K (1985) Two modes of back-arc spreading. *Geology* 13:475. doi:  
665 10.1130/0091-7613(1985)13<475:TMOBS>2.0.CO;2

666 Tamaki K, Pisciotto K, Allan J (1990) Site 797. In: Proc. ODP, Init. Repts.  
667 College Station, TX (Ocean Drilling Program), pp 323–421

668 Tatsumi Y, Otofujii Y, MATsuda T, Nohda S (1989) Opening of the Sea of  
669 Japan back-arc basin by asthenospheric injection. *Tectonophysics* 166:317–329.  
670 doi: 10.1016/0040-1951(89)90283-7

671 Thomson WT (1950) Transmission of elastic waves through a stratified  
672 medium. *J Appl Phys* 21:89–93; 89

673 Van Horne A, Sato H, Ishiyama T (2017) Evolution of the Sea of Japan  
674 back-arc and some unsolved issues. *Tectonophysics* 710–711:6–20. doi:  
675 10.1016/j.tecto.2016.08.020

676 Yoshizawa K, Miyake K, Yomogida K, et al (2010) 3D upper mantle  
677 structure beneath Japan and its surrounding region from inter-station dispersion

678 measurements of surface waves. *Phys Earth Planet Inter* 183:4–19. doi:

679 10.1016/j.pepi.2010.02.012

680 Yu Y, Song J, Liu KH, Gao SS (2015) Determining crustal structure beneath

681 seismic stations overlying a low-velocity sedimentary layer using receiver

682 functions. *J Geophys Res B Solid Earth* 120:3208–3218. doi:

683 10.1002/2014JB011610

684 Yuan X, Kind R, Li X, Wang R (2006) The S receiver functions: Synthetics

685 and data example. *Geophys J Int* 165:555–564. doi: 10.1111/j.1365-

686 246X.2006.02885.x

687 Zhang R, Wu Q, Sun L, et al (2014) Crustal and lithospheric structure of

688 Northeast China from S-wave receiver functions. *Earth Planet Sci Lett* 401:196–

689 205. doi: 10.1016/j.epsl.2014.06.017

690 Zheng Y, Shen W, Zhou L, et al (2011) Crust and uppermost mantle beneath

691 the North China Craton, northeastern China, and the Sea of Japan from ambient

692 noise tomography. *J Geophys Res* 116:B12312. doi: 10.1029/2011JB008637

693

694

695 **Figure legends**

696

697 **Figure 1.** Tectonic setting of the study area and station arrangement. Red squares denote  
698 observation sites where broadband seismometers were deployed.

699

700 **Figure 2.** Examples of teleseismic S waveforms recorded by a broadband ocean-bottom  
701 seismometer. The waveforms are bandpass-filtered between 0.03–0.1 Hz. Zero on the  
702 time axis corresponds to the theoretical S arrivals.

703

704 **Figure 3.** S-receiver functions for each site. Black, red, and green traces represent  
705 rejected, accepted, and stacked receiver functions, respectively.

706

707 **Figure 4** Reference velocity models. Red, blue, and green lines represent the reference  
708 models for YMB3, JS4, and JPB4, respectively. Solid lines represent the S-wave  
709 velocity. Dashed lines represent the P-wave velocity. (a) Overall view. (b) Enlarged  
710 view for the shallow portion.

711

712 **Figure 5.** Inversion results for station YMB3 located at the Yamato Basin. (a) Posterior

713 probability of the number of layers. (b) Frequency distribution of predicted S-receiver  
714 functions. The background color shows the distribution, and the green line denotes the  
715 observed S-receiver function. (c, d) Posterior marginal probability of the S-wave  
716 velocity at each depth bin: (c) enlarged view for the seafloor sediment; (d) overall view.  
717 The background color shows the probability. Blue solid and black dashed lines denote  
718 the median and reference models, respectively.

719

720 **Figure 6.** The same as Figure 5 but for station JS4 located at the Yamato Rise.

721

722 **Figure 7.** The same as Figure 5 but for station JPB4 located at the Japan Basin.

723

724 **Figure 8.** Forward model experiments with (a–d) simple and (e–h) more realistic  
725 velocity models. (a, e) S-wave velocity ( $V_s$ ) models tested through forward modeling.  
726 The models have an additional water layer with a 3-km thickness, although not shown  
727 in these panels. (b–d, f–h) Synthetic S-receiver functions calculated through different  
728 damping: (b, f) without damping, (c, g) with a damping factor of 0.001, and (d, h) with a  
729 damping factor of 0.01. Line colors correspond to those in (a) and (e).

730

731 **Figure 9.** Radial-component responses of a sediment layer overriding a half space. (a)  
732 Algebraic expression given by Equation 18. Color notation is the same as Figure 8a.  
733 (b) Numerical results.

734

735 **Figure 10.** Time-to-depth converted and stacked S-receiver functions (S-RFs) for each  
736 station. (a) Stations locations (red squares). (b) The depth-converted, stacked S-RFs.  
737 Positive and negative amplitudes are shaded in red and blue, respectively. The gray  
738 shade represents the 95% confidence interval from bootstrap resampling 1000 times.

739

740 **Figure 11.** Comparison to surface wave tomography model. (a) Seafloor topography  
741 profile. (b) Cross section of S-wave velocity model estimated by surface wave  
742 tomography (Yoshizawa et al. 2010). The shallow portion (< 30 km depth) is masked by  
743 the gray shade because of insufficient resolution with long-period surface waves. Blue  
744 horizons roughly indicate the lithosphere–asthenosphere boundary inferred from the  
745 inversion. Red squares denote station locations. (c) Profile location (red line) and station  
746 locations (red squares).

747

748 **Figure 12.** Schematic illustration of the lithosphere-asthenosphere system across

749 northeastern Japan, the Sea of Japan, and northeastern China.

750

751 **Tables**

752 **Table 1.** Summary of observation

Site name	Tectonic domain	Data availability
JPB4	Japan Basin	2017/07/18–2019/07/27
JPB5	Japan Basin	2018/07/25–2018/10/17
JPB6	Japan Basin	2017/07/18–2019/07/27
YMB3	Yamato Basin	2013/10/18–2015/8/11
YMB4	Yamato Basin	2013/10/18–2014/08/03, 2015/08/11–2016/08/08
JS2	Yamato Basin	2003/08/14–2003/11/15
JS4	Yamato Rise	2002/12/01–2003/11/15

753

754 **Table 2** Velocity models used in forward modeling.

	Vp (km/s)	Vs (km/s)	Density (g/cm <sup>3</sup> )	Thickness (km)
Seawater	1.5	-	1.0	3
Sediment #1	1.5	0.07–0.7	1.3–1.9	0.05

Sediment #2	2.1	0.7	1.9	0.1
Crust #1	4.3	2.5	2.4	3
Crust #2	6.0	3.5	2.7	4
Mantle	8.1	4.6	3.3	-

755

## Figures

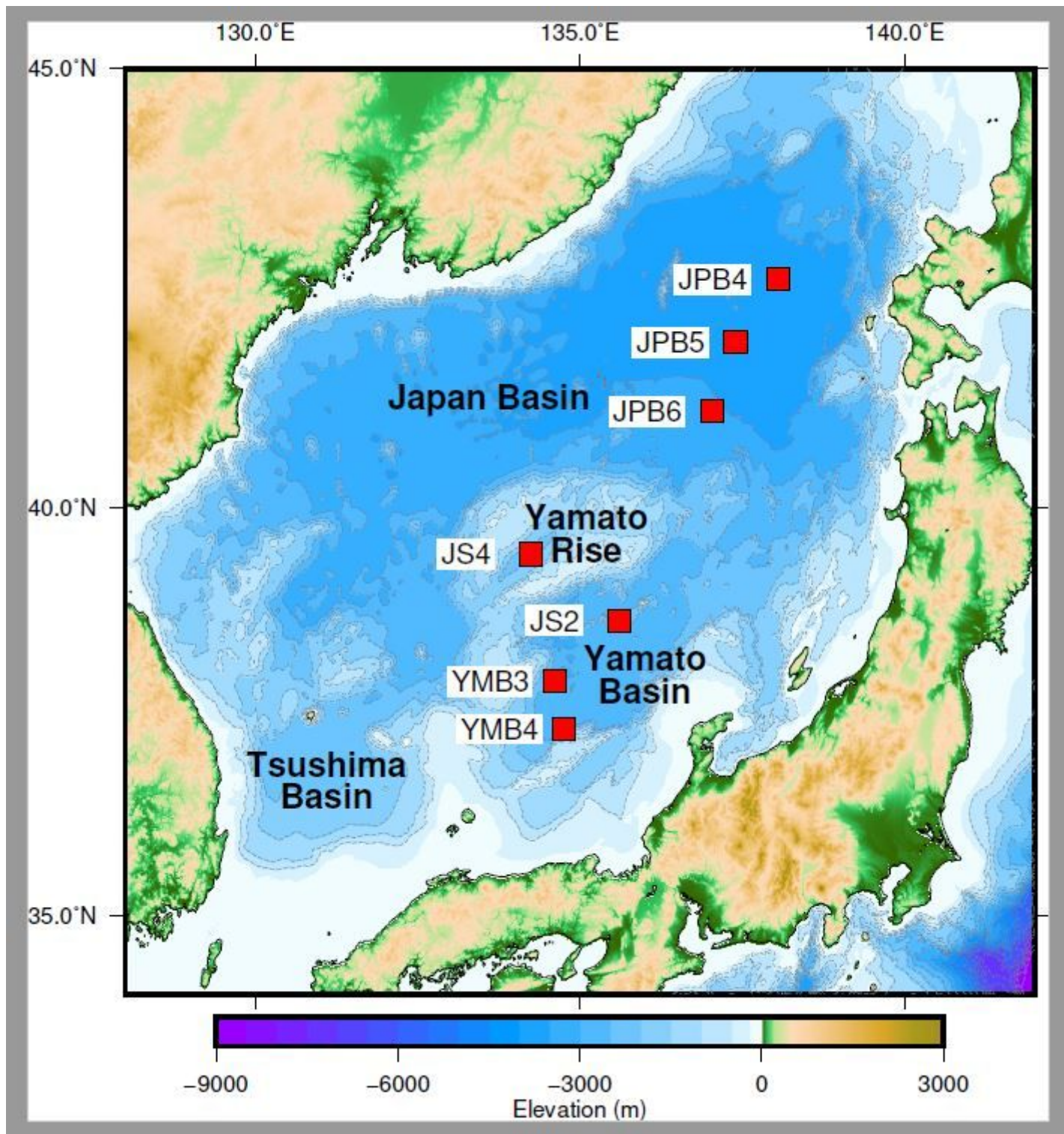
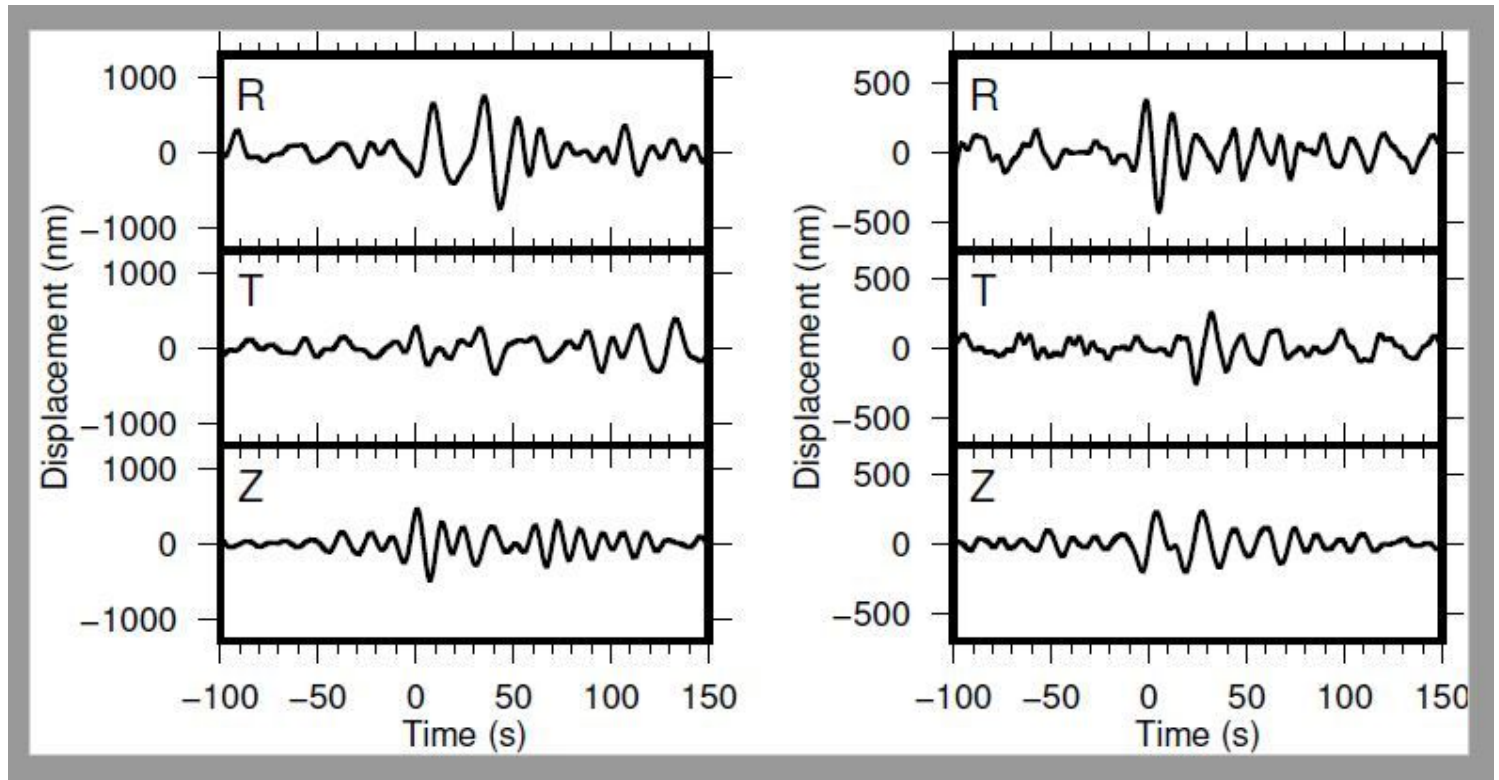


Figure 1

Tectonic setting of the study area and station arrangement. Red squares denote observation sites where broadband seismometers were deployed. Note: The designations employed and the presentation of the material on this map do not imply the expression of any opinion whatsoever on the part of Research

Square concerning the legal status of any country, territory, city or area or of its authorities, or concerning the delimitation of its frontiers or boundaries. This map has been provided by the authors.



**Figure 2**

Examples of teleseismic S waveforms recorded by a broadband ocean-bottom seismometer. The waveforms are bandpass-filtered between 0.03–0.1 Hz. Zero on the time axis corresponds to the theoretical S arrivals.

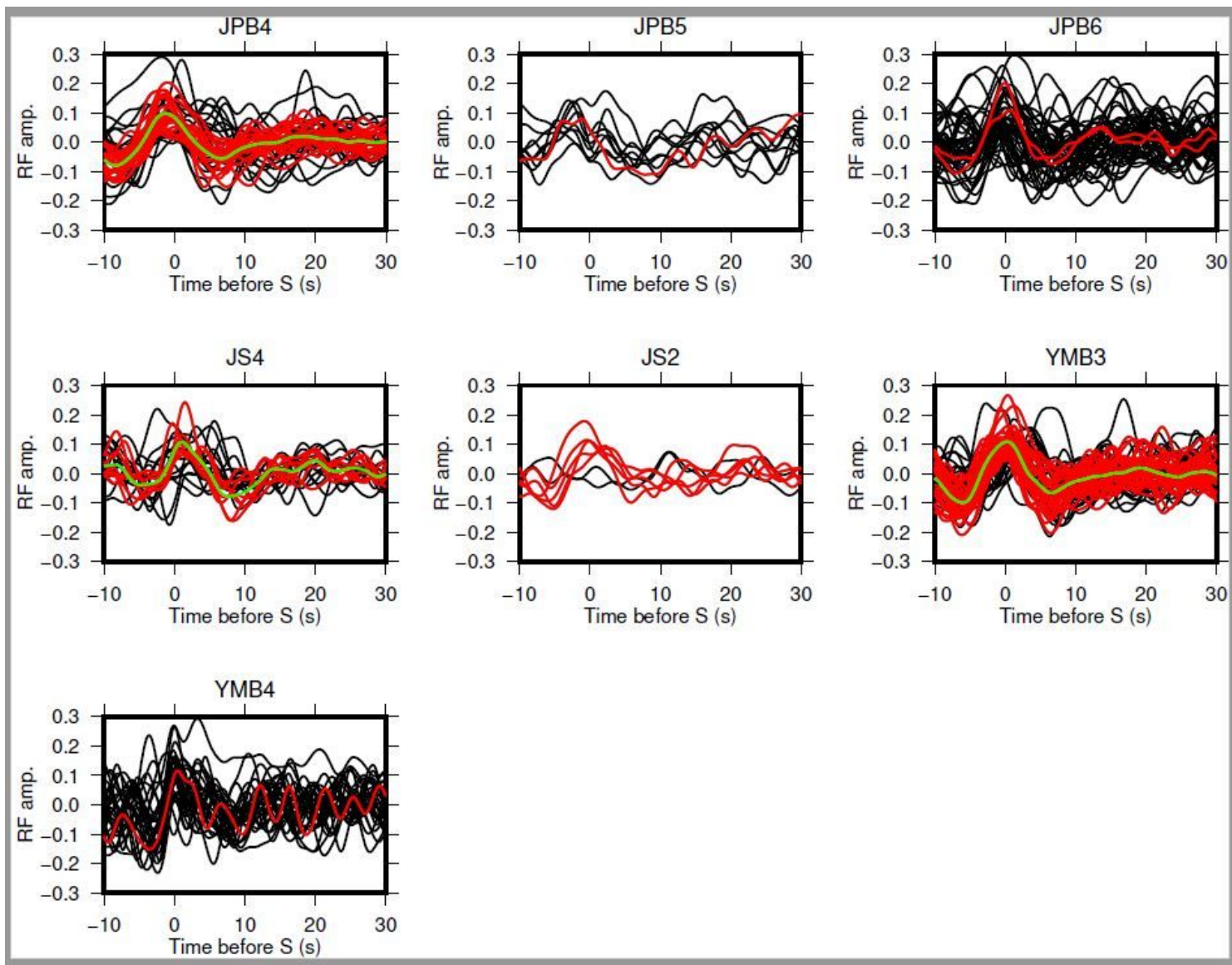


**Figure 3**

S-receiver functions for each site. Black, red, and green traces represent rejected, accepted, and stacked receiver functions, respectively.

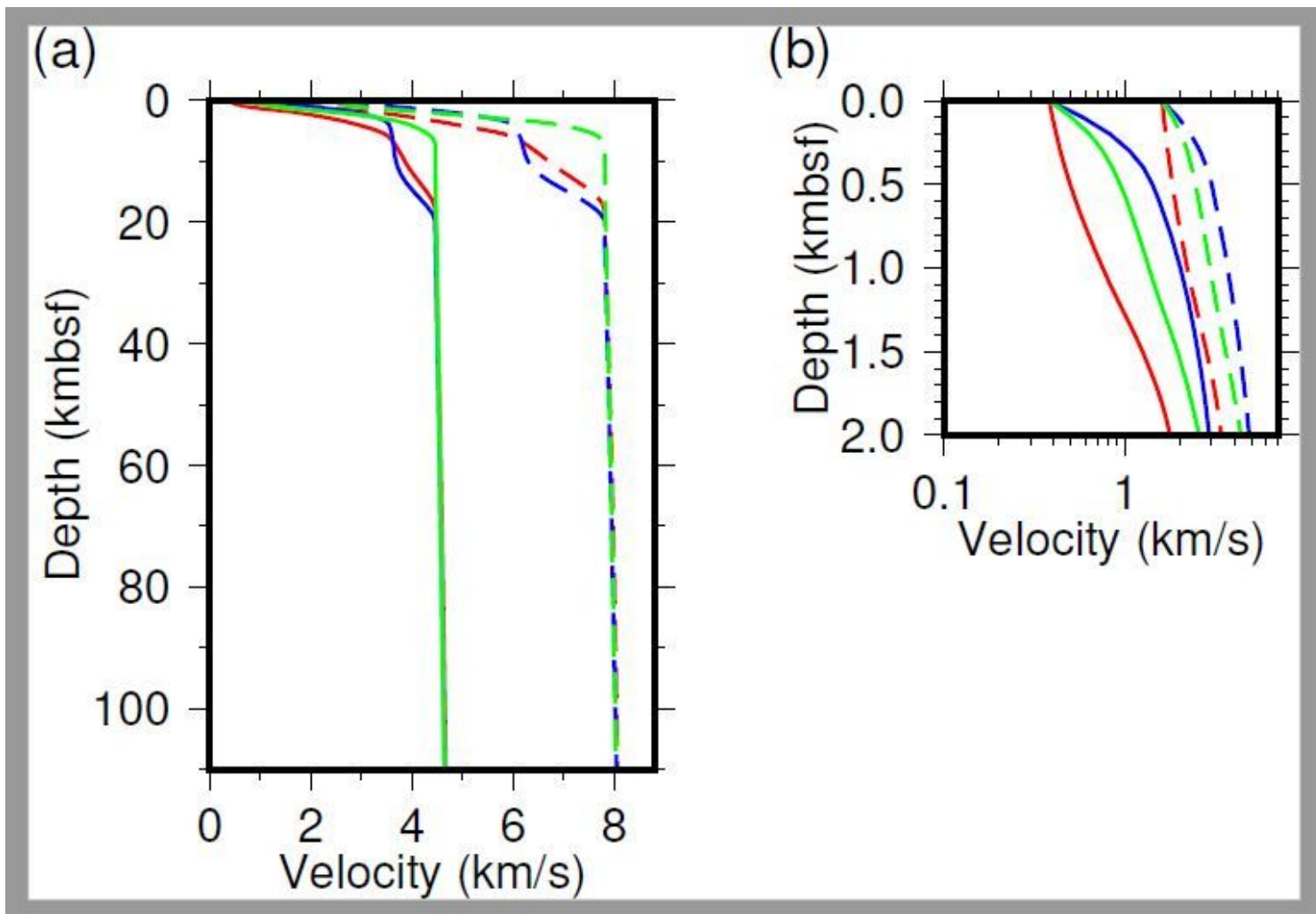


**Figure 4**

Reference velocity models. Red, blue, and green lines represent the reference models for YMB3, JS4, and JPB4, respectively. Solid lines represent the S-wave velocity. Dashed lines represent the P-wave velocity. (a) Overall view. (b) Enlarged view for the shallow portion.

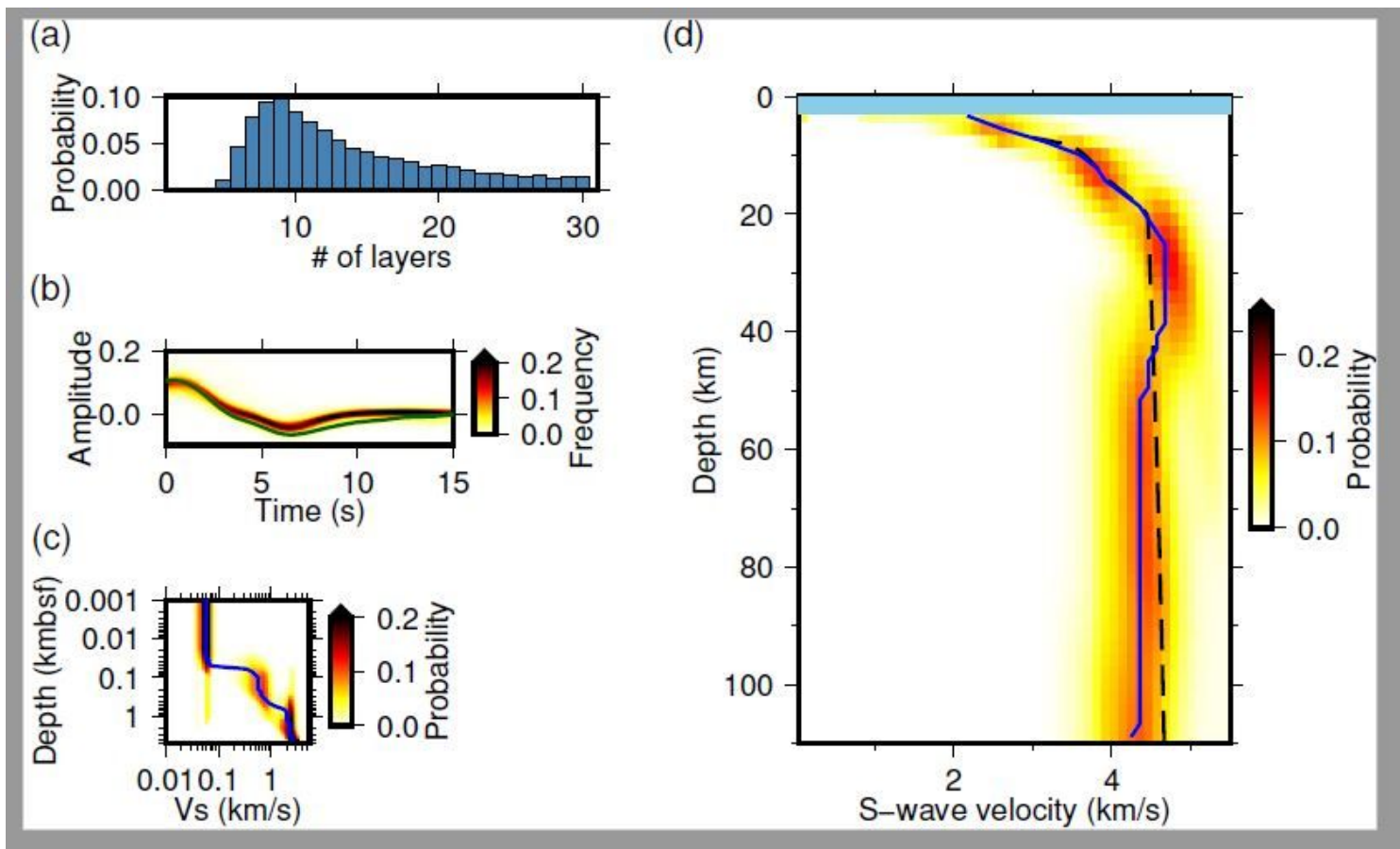


**Figure 5**

Inversion results for station YMB3 located at the Yamato Basin. (a) Posterior probability of the number of layers. (b) Frequency distribution of predicted S-receiver functions. The background color shows the distribution, and the green line denotes the observed S-receiver function. (c, d) Posterior marginal probability of the S-wave velocity at each depth bin: (c) enlarged view for the seafloor sediment; (d) overall view. The background color shows the probability. Blue solid and black dashed lines denote the median and reference models, respectively.

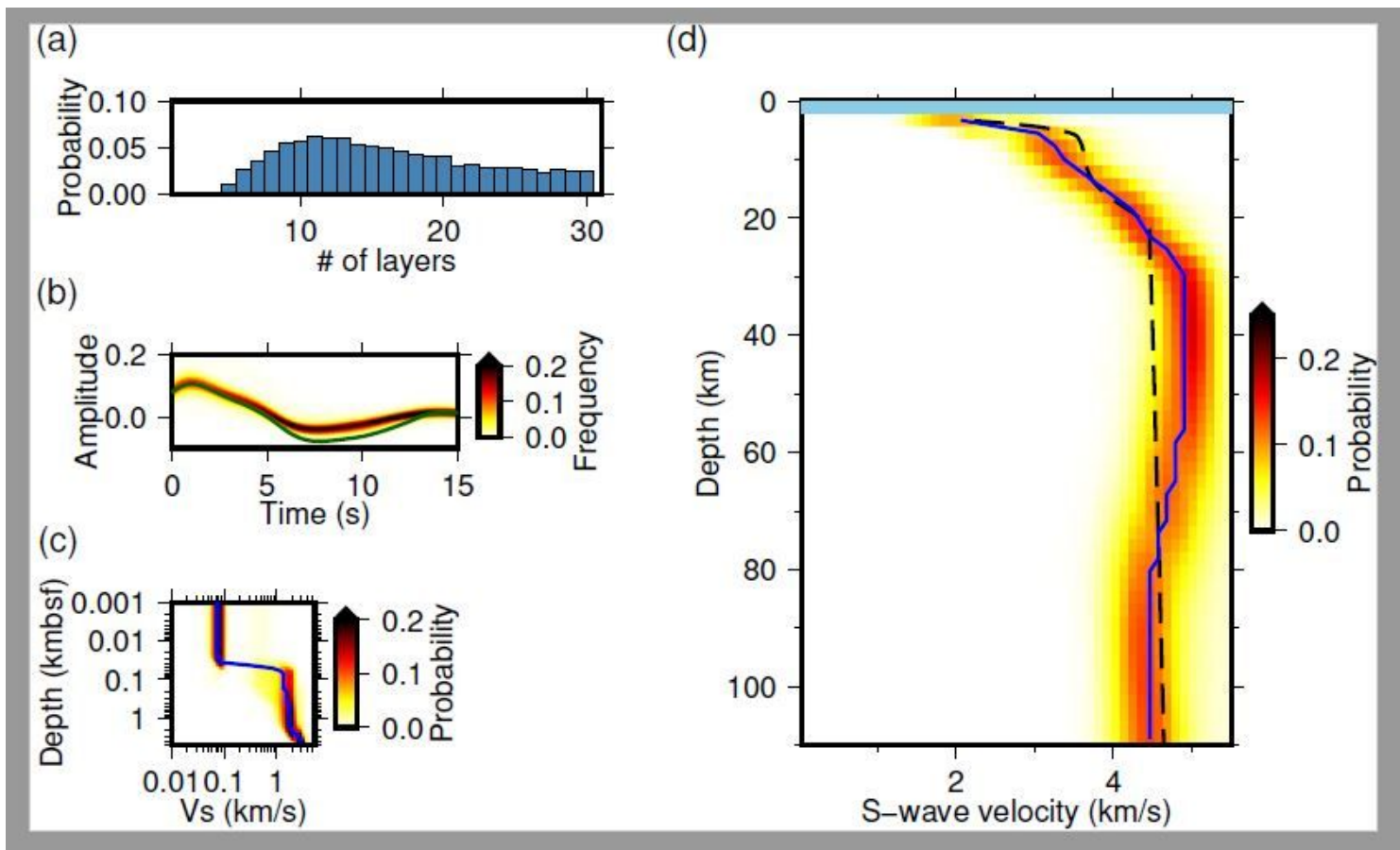


Figure 6

The same as Figure 5 but for station JS4 located at the Yamato Rise.

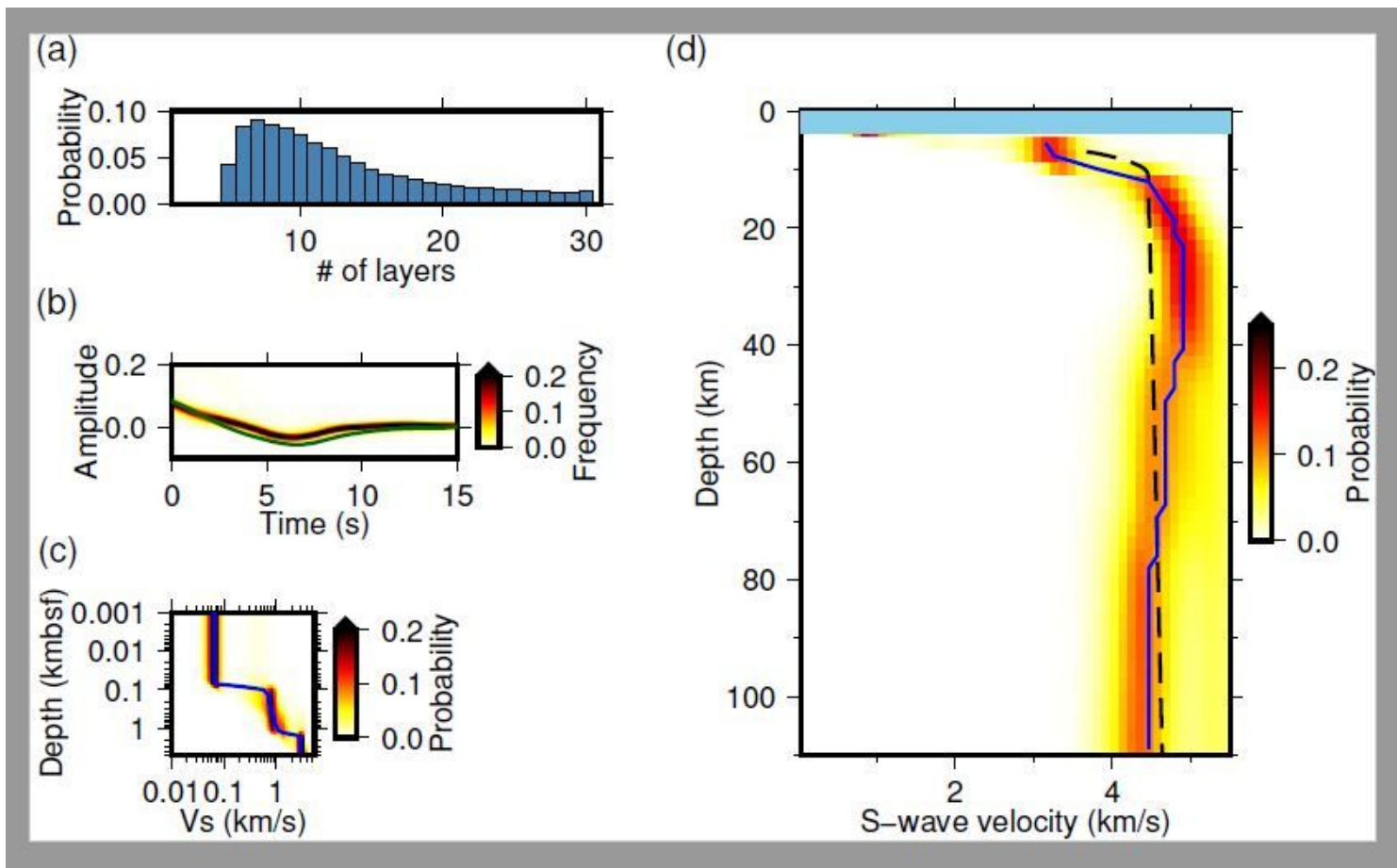
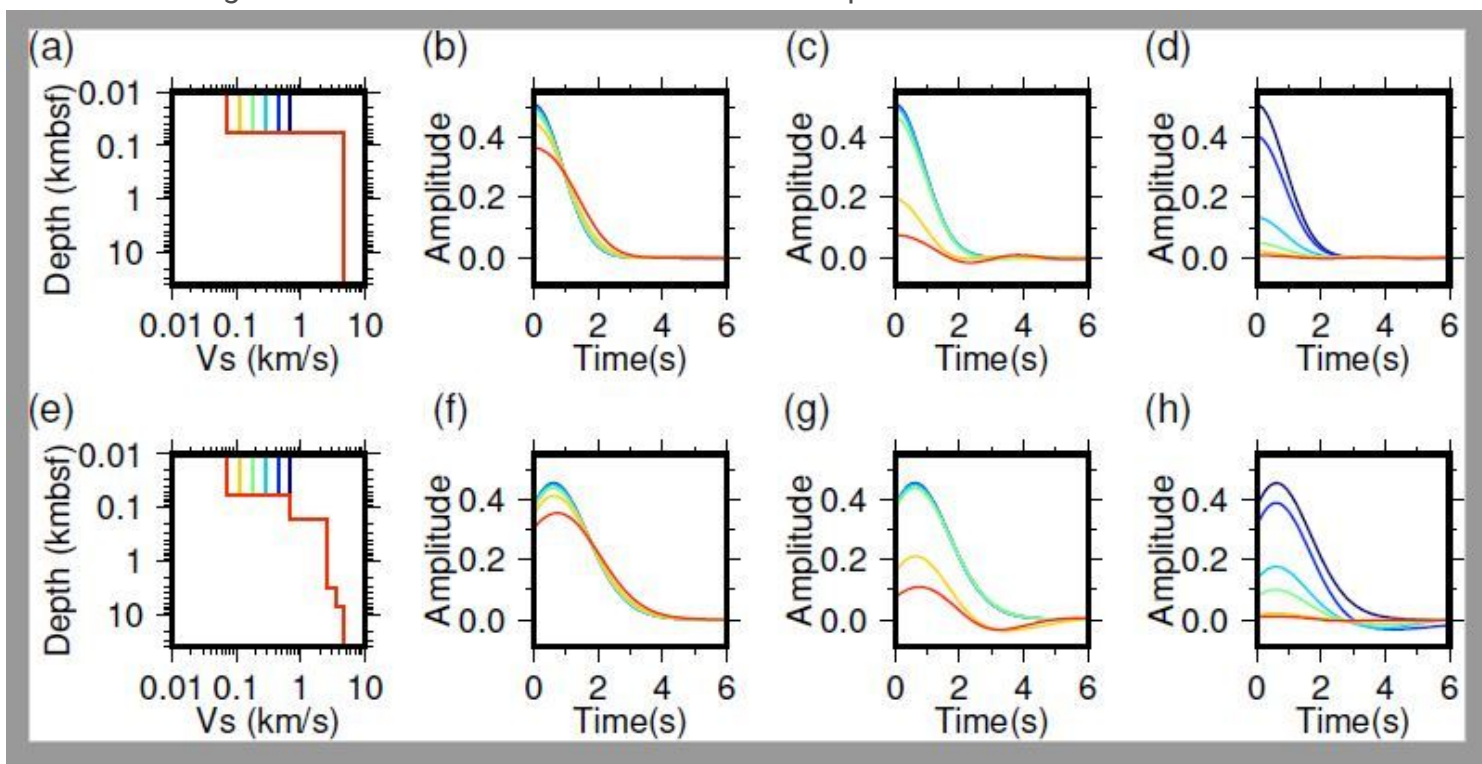


Figure 7

The same as Figure 5 but for station JPB4 located at the Japan Basin.



**Figure 8**

Forward model experiments with (a–d) simple and (e–h) more realistic velocity models. (a, e) S-wave velocity ( $V_s$ ) models tested through forward modeling. The models have an additional water layer with a 3-km thickness, although not shown in these panels. (b–d, f–h) Synthetic S-receiver functions calculated through different damping: (b, f) without damping, (c, g) with a damping factor of 0.001, and (d, h) with a damping factor of 0.01. Line colors correspond to those in (a) and (e).

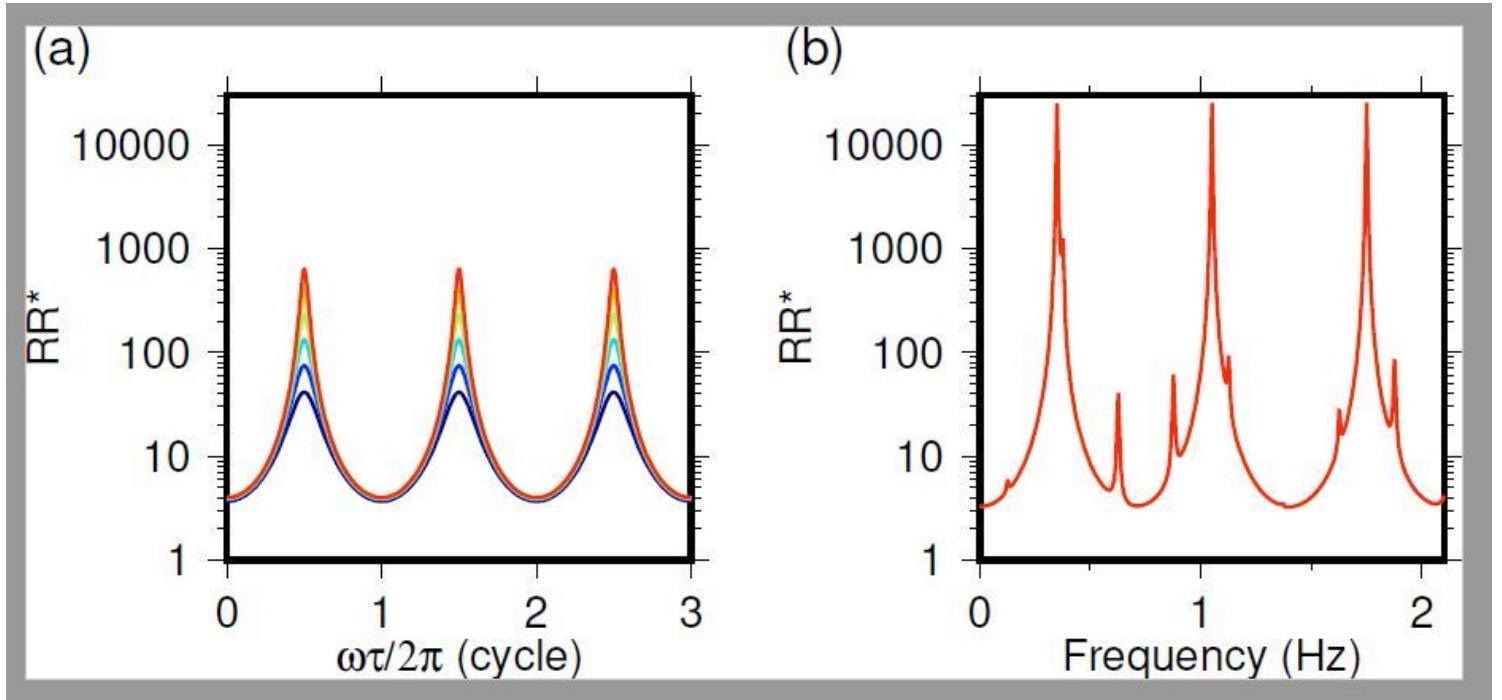


**Figure 9**

Radial-component responses of a sediment layer overriding a half space. (a) Algebraic expression given by Equation 18. Color notation is the same as Figure 8a. (b) Numerical results.

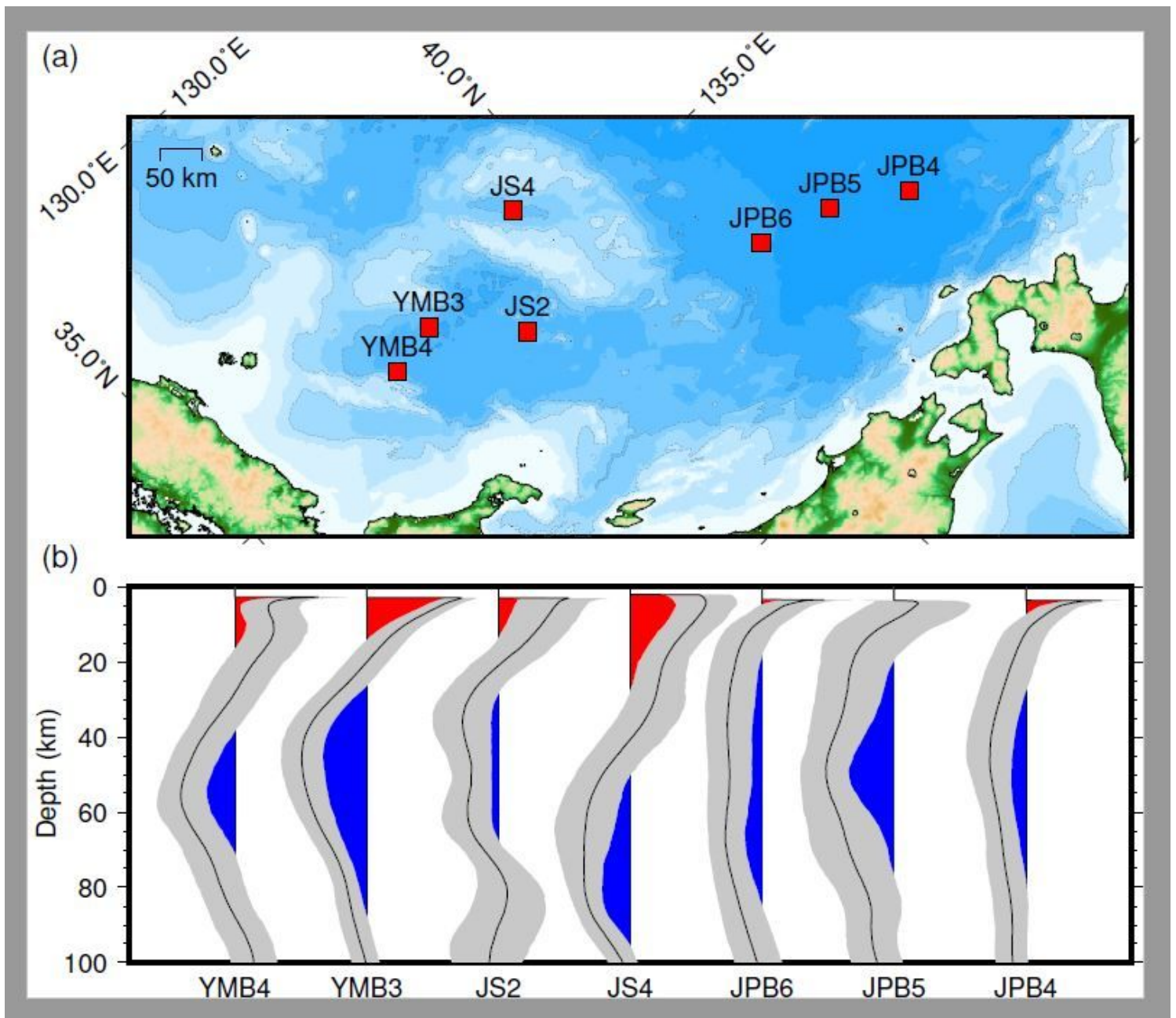


**Figure 10**

Time-to-depth converted and stacked S-receiver functions (S-RFs) for each station. (a) Stations locations (red squares). (b) The depth-converted, stacked S-RFs. Positive and negative amplitudes are shaded in red and blue, respectively. The gray shade represents the 95% confidence interval from bootstrap resampling 1000 times. Note: The designations employed and the presentation of the material on this map do not imply the expression of any opinion whatsoever on the part of Research Square concerning the legal status of any country, territory, city or area or of its authorities, or concerning the delimitation of its frontiers or boundaries. This map has been provided by the authors.

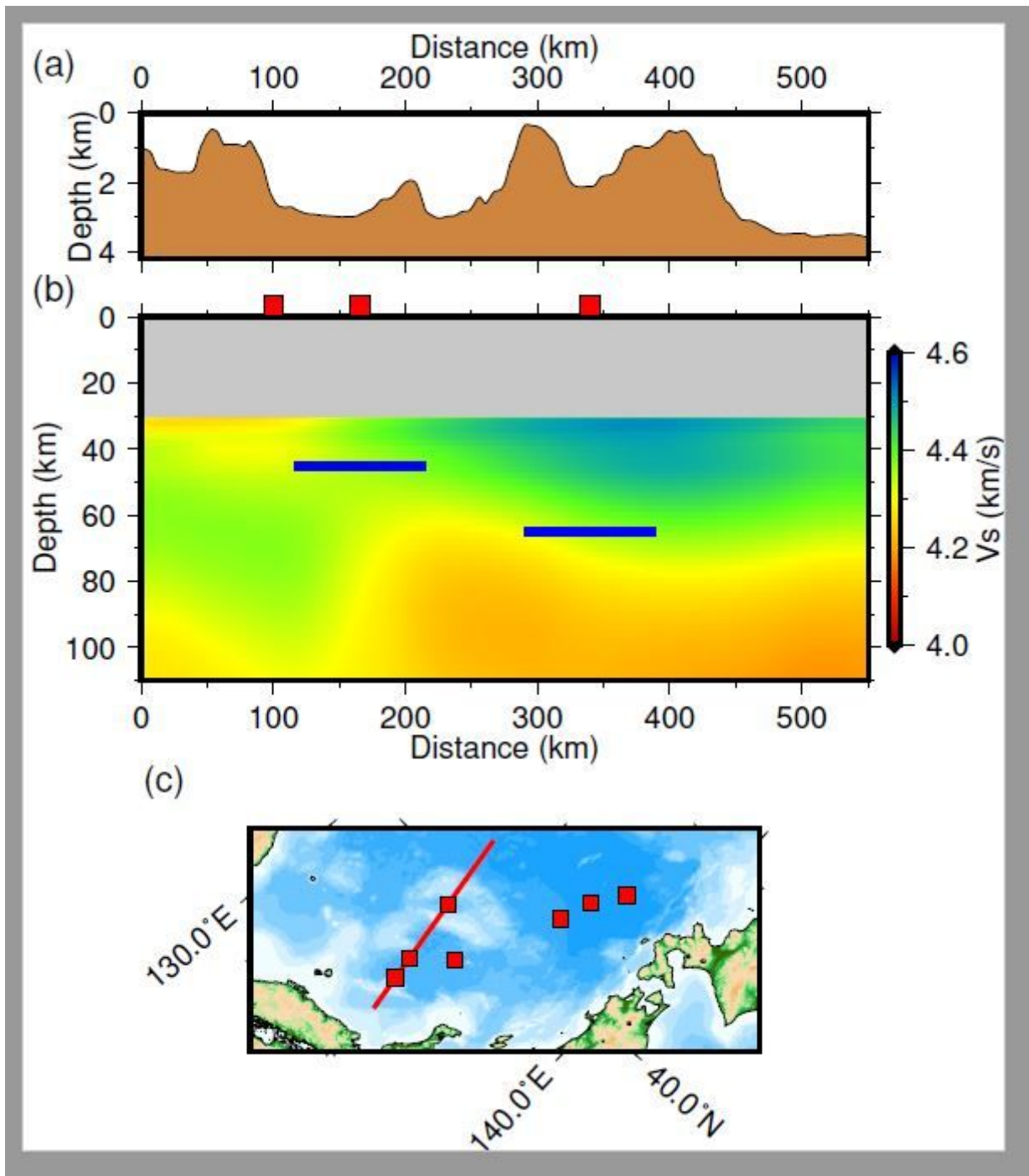


**Figure 11**

Comparison to surface wave tomography model. (a) Seafloor topography profile. (b) Cross section of S-wave velocity model estimated by surface wave tomography (Yoshizawa et al. 2010). The shallow portion ( $< 30$  km depth) is masked by the gray shade because of insufficient resolution with long-period surface waves. Blue horizons roughly indicate the lithosphere–asthenosphere boundary inferred from the inversion. Red squares denote station locations. (c) Profile location (red line) and station locations (red squares).

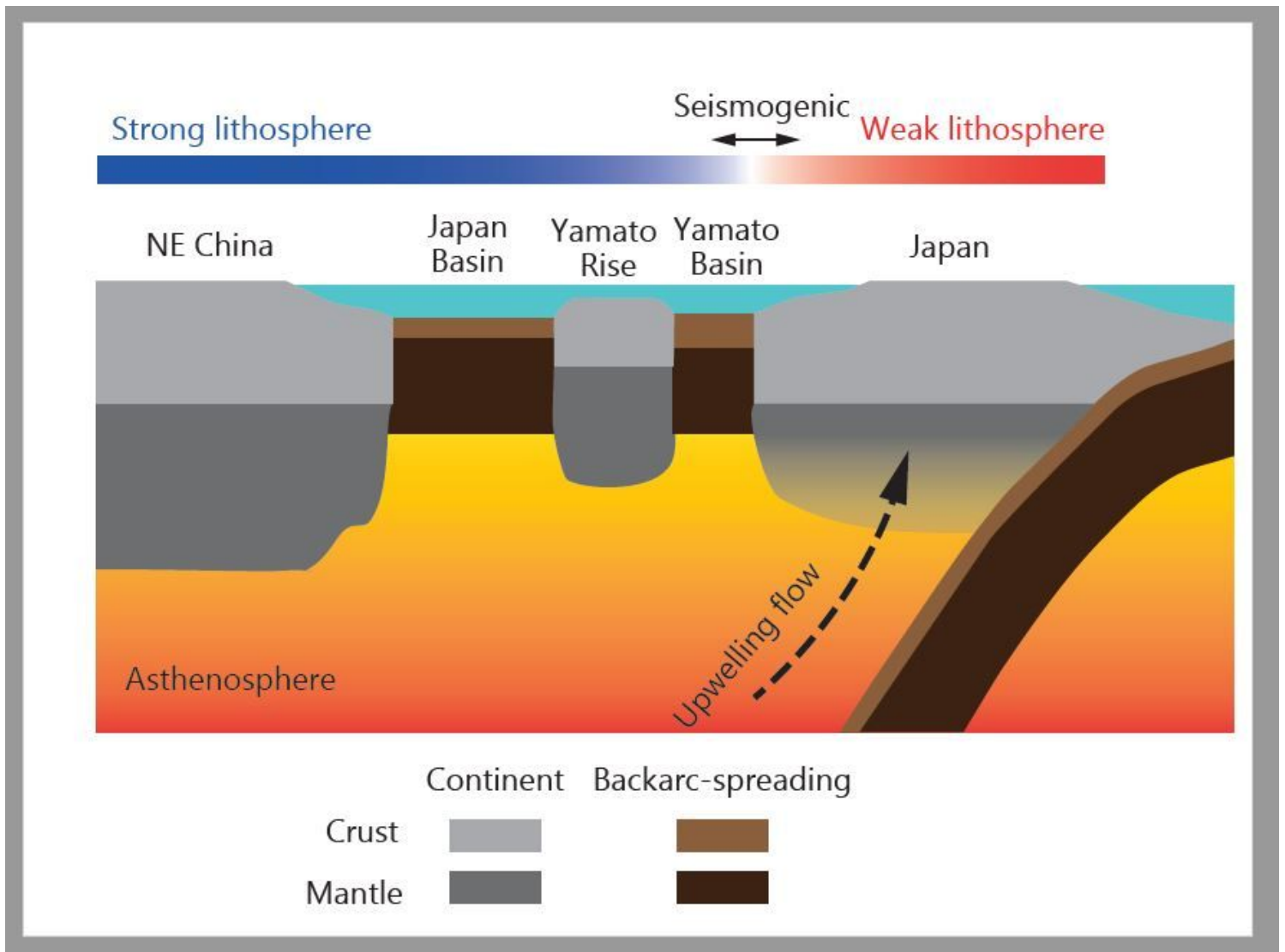


**Figure 12**

Schematic illustration of the lithosphere-asthenosphere system across northeastern Japan, the Sea of Japan, and northeastern China.

## Supplementary Files

This is a list of supplementary files associated with this preprint. Click to download.

- [Appendix1.docx](#)
- [graphicalabst.png](#)